

Application of Wave-current coupled Sediment Transport Models with Variable Grain Properties for Coastal Morphodynamics: A Case Study of the Changhua River, Hainan

Yuxi Wu¹, Enjin Zhao¹, Xinwen Li², Shiyu Zhang²

5 ¹College of Marine Science and Technology, China University of Geosciences, Wuhan 430074, China.

²Haikou Marine Geological Survey Center, China Geological Survey, Haikou 570100, China

Correspondence to: Enjin Zhao (zhaoej@cug.edu.cn)

Abstract. This study presents an integrated sand transport model that accounts for both wave and current actions, along with non-constant grain properties, to investigate sediment dynamics in the lower reaches of rivers. Taking the downstream and estuary of the Changhua River in Hainan Island as a case study, topographic data and sediment sampling were conducted in the field, complemented by remote sensing techniques. The model was rigorously validated using theoretical and empirical methods, demonstrating excellent agreement with observed suspended sediment concentrations at the Baoqiao Station. The findings indicate significant sediment deposition in the estuary and lower reaches of the Changhua River, influenced by a combination of hydrodynamic conditions and geological settings. Deposition in the estuary is primarily affected by the northeast-southwest coastal currents and wave action, while deposition in the river channel is associated with river constriction and variations in flow velocity. Regardless of whether it is the dry or wet season, the residual current in the study area flows towards Beili Bay, indicating that the sediment in the lower reaches of the Changhua River will be influenced by the residual flow, moving southward.

1 Introduction

20 Hainan Island has an extensive coastline, making marine economy a crucial source of its economic prosperity (Feng et al., 2021; Jin et al., 2008; Fang et al., 2021). Changhua River is the second largest river in Hainan in terms of its basin area (Zhang et al., 2020; Zeng and Zeng, 1989), which flowing uniquely into the Beibu Gulf in the northwest of Hainan Island, serves as a crucial water source for the region, supporting irrigation, power generation, and water supply (Yang et al., 2013; Wang et al., 2023). The Changhua River is divided into upper, middle, and lower reaches based on its natural geographical characteristics: the upper reaches extend from the source to Poyang with a length of 79 kilometers and an average gradient of 14.87 %; the middle reaches run from Poyang to Chahe with a total length of 84 kilometers, which includes a significant drop at Guangba in Dongfang County, and generally feature a milder gradient; the lower reaches start from Chahe down to the river's mouth at Changhua Port, spanning 39 kilometers with an average gradient of 0.41 %, leading to a broad river plain (Fig. 1). Characterized by a gentler gradient and slower flow, the lower reaches are where the river's capacity to carry

30 sediment decreases, leading to increased sediment deposition. Currently, the issues related to water and sediment in the lower reaches of Changhua River are primarily divided into studies on sediment composition and sediment transport (Zhang et al., 2006; Wu et al., 2012; Zhu et al., 2020; Gao et al., 2014; Wang et al., 2022; Zhao et al., 2021). About the sediment concentration information, the annual sediment concentration of the Changhua River is recorded as 0.173 kg/m^3 , with an average annual sediment discharge of 782,000 tons, classifying it as a river with relatively low sediment load. From 2013 to
35 2021, the average sediment concentration at Baoqiao Station in the lower reaches of the Changhua River was determined to be 0.1227143 kg/m^3 .

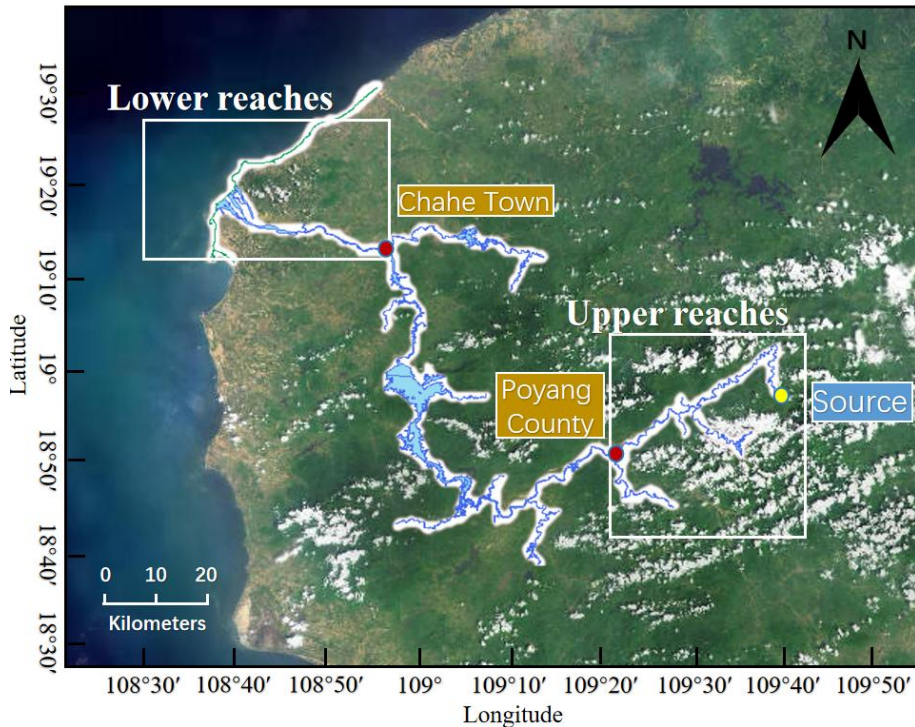


Figure 1: Division of the Upper, Middle, and Lower Reaches of the Changhua River (map origination: <https://hainan.tianditu.gov.cn/>)

40 In the lower reaches of rivers, sediment dynamics are influenced by both water flow and waves, which are crucial for understanding the changes in estuarine and nearshore ecosystems, shoreline evolution, and the development of ocean resources. With the rapid advancement of computational technologies, significant progress has been made in sediment modeling studies, particularly in modeling sediment transport in the lower reaches of rivers where wave and current interactions are considered.

45 Researchers have developed a variety of computational models to simulate sediment transport processes in the lower reaches. These models include one-dimensional (1D), two-dimensional (2D), and three-dimensional (3D) hydrodynamic and sediment transport models that describe the flow and sediment movement in rivers, lakes, and coastal areas (Papanicolaou et

al., 2010). 1D models are typically used for large-scale, long-term sediment transport issues (Thomas and Prashum, 1977; Holly and Rahuel, 1990; Papanicolaou et al., 2004), while 2D and 3D models are more suitable for simulating specific flow and sediment transport conditions, especially in the lower reaches and estuary areas (Lee et al., 1997; Jia and Wang, 1999; Gessler et al., 1999; Wu et al., 2000; Blumberg and Mellor, 1987).

Traditional sediment transport models have predominantly focused on the dynamics of water flow, with wave action often addressed in a simplified manner or neglected altogether (Bakhtyar et al., 2009; Lee et al., 1997; Spasojevic and Holly, 1990; Bai et al., 2017). We need more accurate and comprehensive models that can describe and predict sediment behavior under the combined action of waves and currents, especially for rivers with low sediment concentration. In this context, the Van Rijn formula emerges as a critical tool for enhancing the precision of sediment transport modeling (Van-Rijn, 1984). Originally formulated to calculate the transport of bed load and suspended sediment, the Van Rijn formula has been adapted over time to accommodate the intricate interplay between waves and currents. Its empirical nature, grounded in extensive field and laboratory data, allows for a nuanced representation of sediment dynamics in coastal environments. The recent applications of the Van Rijn formula in computational models have further expanded its utility, providing a robust framework for analyzing sediment behavior in scenarios characterized by wave and current interactions (Chen et al., 2024; Michel et al., 2023; Addison – Atkinson et al., 2024).

With the advancement of computational technologies and the development of remote sensing techniques, researchers have begun to incorporate the complex interactions of waves and currents into sediment transport modeling (Han et al., 2022; Liu et al., 2014; Vinzon et al., 2023). These models not only consider the velocity and direction of water flow but also account for the energy input from waves, wave form changes, and the shear forces generated by wave-current interactions. Studies have shown that sediment movement under wave action is not only influenced by the shear stress of the water flow but also by the liquefaction and mass transport of bottom sediment caused by waves (Niu et al., 2023). Additionally, the physical properties of sediment, such as particle size distribution, concentration, and sedimentation rates, are crucial factors affecting sediment behavior under the combined influence of waves and currents (Constant et al., 2023; Salgado Terêncio et al., 2023). Despite the progress made, sediment modeling under the combined action of waves and currents still faces many challenges. For example, how to better simulate sediment transport in complex turbulent flows, the coupling of flow and sediment transport, and the transport of non-uniform sediment still require further research. Moreover, model input and calibration also require more field data and experimental validation to ensure the reliability and applicability of the models. To verify the effectiveness of wave-current coupled sediment model in rivers with low sediment concentration, we take Changhua River in Hainan Province as an example to verify it.

To sum up, the sediment simulation considering only water flow can no longer meet the accuracy of sediment prediction, and there are still limitations in the verification of sediment simulation considering the interaction of waves and water flow. Most river sediment models do not study rivers with small sediment concentration separately and lack in-situ observation, so the accuracy of the models needs further verification. Additionally, due to the small scope of the lower reaches of Changhua River, the existing terrain extraction methods are not enough to provide terrain data with appropriate accuracy. Moreover,

the sediment concentration of Changhua River is not large and the existing research data are limited. In the absence of topographic data and sediment data, a complete and mature sediment transport model has not been established in the lower reaches of Changhua River so far. In this paper, we take Changhua River in Hainan Province as a representative of the river with less sediment, and consider the sediment deposition under the combined action of waves and currents. Based on the measured topographic data and sediment sampling data, the bed load and suspended sediment load are calculated respectively by Van Rijn model, and the sediment model is established. The in-situ observation of suspended sediment concentration are used to verify the model and analyze the sediment deposition in the lower reaches channel and estuary.

2 Research Methods

2.1 Combined Wave and Current Sand Transport Model

This study assumes the sediment to be non-viscous, and the sediment deposition model utilizes the results from the hydrodynamic model as open boundary driving forces. The model definition in the sand transport model is assumed as combined current and waves, calculating the bed load and suspended load separately. Bed load typically occurs close to the bed, while suspended load can be transported at various levels within the water column. Sediment particles begin to move and may become suspended when the bed shear stress exerted by waves and currents exceeds a critical threshold. The equations adopt Van Rijn model. Van Rijn proposed the following models for sediment transport of bed load and suspended load, which are suitable for sediment transport calculation under wave action (Van Rijn, 1984). The Van Rijn model formula is derived based on a set of variables that are crucial for understanding sediment transport dynamics, particularly in the context of rivers and coastal waters. These variables include:

$$q_s = f_{sl} \cdot C_a \cdot u_*^2 \quad (1)$$

$$q_b = 0.053 \frac{M^{2.1}}{D_*^{0.3}} \sqrt{(s-1)g \cdot d_{50}^3} \quad (2)$$

$$f_{sl} = C' \cdot \left(\frac{u_*}{u_{*c}} \right)^m \quad (3)$$

$$u_* = \sqrt{\frac{\tau}{\rho}} \quad (4)$$

$$M = \left(\frac{u_{f,c}}{u_{f,c}} \right) - 1 \quad (5)$$

$$u_{f,c} = \sqrt{\theta_c (s-1)g \cdot d_{50}} \quad (6)$$

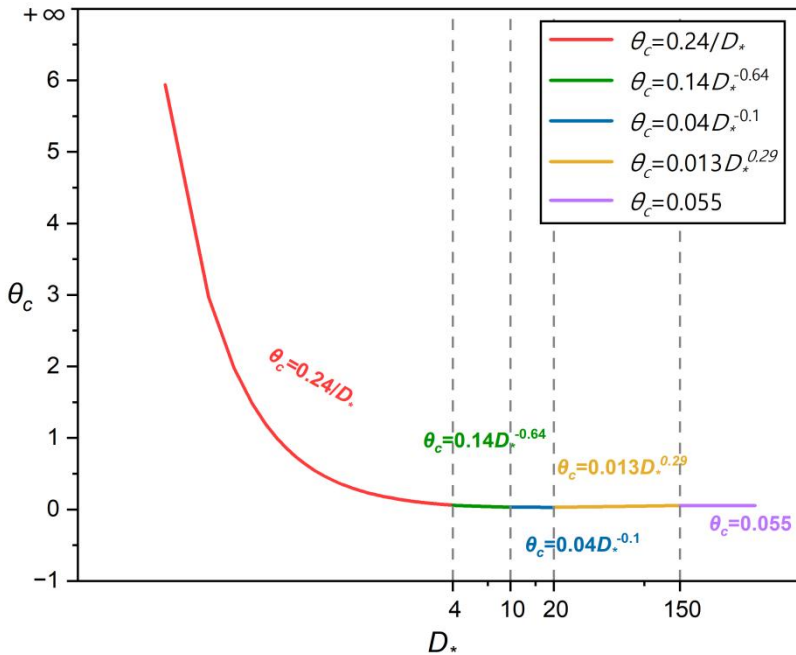
$$u_{f'} = V \sqrt{\frac{g}{C'}} \quad (7)$$

$$C' = 18 \log \left(\frac{4h}{d_{50}} \right) \quad (8)$$

$$D_* = d_{50}^3 \sqrt{\frac{(s-1)g}{\nu^2}} \quad (9)$$

Where q_b is the bed load transport rate; q_s is the suspended load transport rate; M is the non-dimensional transport stage parameter; $u_{f,c}$ is the critical friction velocity, which under the current; θ_c is the critical Shield parameter; $u_{f'}$ is the effective friction velocity; C' is the Chezy number originationg from skin friction; D_* is the non-dimensional particle parameter; C_a is the kinematic viscosity and approximately equal to 10^{-6} m²/s for water; u_* is the bed concentration; τ is the friction velocity; τ_* is the shear stress at the bed surface; ρ is the density of water; m is empirical exponent.

In the context of the Van Rijn model, the non-dimensional particle parameters can influence the value of the critical Shield parameter. For example, as the particle size increases, the critical Shields parameter may also increase because larger particles require more force to overcome gravity and initiate motion. Similarly, changes in fluid properties or flow conditions can affect both the non-dimensional particle parameters and the critical Shield parameter. Instead of using a constant critical Shields parameter θ_c , Van Rijn assumes the following variation as a function of D_* , see Fig. 2.



120 **Figure 2: Relations for determination of critical Shields stress**

After calculating the bed load and suspended load separately, the Bijker model is used to calculate the total sediment transport rate (Bijker, E.W. 1967), which includes both bed load and suspended load components. and the formula is as follows:

$$q_t = q_s + q_b = q_b(1 + 1.83Q) \quad (10)$$

125
$$Q = A \left(\frac{I_1}{I_2} \right) + I_2 \ln \left(\frac{z^*}{r} \right) = \frac{h}{r} \left(\frac{I_1}{I_2} \right) + I_2 \ln \left(\frac{w}{rku_{f,wc}} \right) \quad (11)$$

$$u_{f,wc} = u_{f,c} + \sqrt{u_{f,c}^2 + 2 \cdot \frac{v^2}{V}} \quad (12)$$

$$I_1 = \int_0^h \frac{u(z)}{w} dz, \quad I_2 = \int_0^h \frac{u(z)}{w} \ln \left(\frac{h-z}{d_{50}} \right) dz, \quad (13)$$

Where q_t is the total sediment transport rate; Q is a dimensionless factor that accounts for the effect of waves on the bed load transport; h represents the water depth; r is the bed roughness; I_1 and I_2 are Einstein's integrals, which are functions of the dimensionless reference level A and the dimensionless roughness height z^* ; w is the settling velocity of the suspended sediment; k is von Karman's constant; $u_{f,wc}$ is the shear velocity under the influence of combined waves and current; v is the amplitude of the wave-induced oscillatory velocity at the bottom; V is the depth-averaged flow velocity; $u(z)$ is the flow velocity profile at a height z above the bed.

130

2.2 Influences of Waves and Currents

135 The influence of sediment transport model on water flow has been widely studied and applied (Papanicolaou et al., 2010), including sediment transport mechanisms, the establishment of the boundary layer, modifications to bed morphology, and the vertical distribution of suspended sediment. However, the theory and application of wave action are not mature compared with water flow. This chapter emphasizes the motion equation and boundary condition equation adopted by wave action in the sediment transport model in this paper.

140 The model of sediment transport to calculate the influence of the waves usually through a comprehensive consideration of various factors that encapsulate the impact of waves on sediment transport. The typical models incorporate the nonlinear characteristics of wave motion, net mass transport induced by waves, turbulence generated by wave breaking, the temporal evolution of the boundary layer due to combined wave and current action, contributions to turbulence from three sources (wave boundary layer, mean flow, and wave breaking), and the influence of wave-formed ripples on flow and sediment transport. A suite of wave theories, such as Stokes and Cnoidal theories, are employed to describe wave motion across

145

different hydrodynamic conditions. Additionally, the model accounts for the calculation of turbulence viscosity due to wave breaking, and the equations to compute the shear stress resulting from wave motion are well represented. These complex interactions and processes are articulated through a series of mathematical equations and empirical formulas, enabling the model to accurately simulate the process of sediment transport under the dual influence of waves and current. In this paper, the specific formulas of the wave motion are as follows:

Table 1 Formulas of the wave motion in the sand transport model

Item	Method	Equation
Wave Energy Dissipation	Battjes and Janssen (1978)	$D = \frac{\gamma_1 g H^2}{\gamma_2 k} \tanh(\gamma_2 k h)$
Wave Boundary Layer Thickness	Empirical formula	$\delta = \frac{k}{30} \left(\frac{u_{\max}}{u_*} \right)$
Turbulent Viscosity Induced by Waves	Empirical formula	$\nu_t = C_\mu \frac{u_{\max}^2}{g}$
Shear stress resulting from wave motion	Jørgen Fredsøe (1984)	$\tau = \rho u_*^2$
Wave velocity in shallow water	Cnoidal theory	$c = \sqrt{gh} \left[1 + \frac{H}{h} \left(\frac{1}{k^2} - 0.5 - \frac{3E(x)}{2k^2 K(x)} \right) \right]$ (k is the module of elliptic function. $E(x)$ and $K(x)$ are the first and second complete elliptic integrals)
Wave velocity in deep water	Stokes theory	$c = \sqrt{\frac{g\lambda}{2\pi}}$

After examining the influence of waves and currents on sediment transport modelling, we now turn our attention to the specific characteristics of sediment properties in the study area. Section 2.3 provides a detailed account of these properties, which are essential for understanding the local sediment dynamics and will be crucial for the model's calibration and validation processes.

2.3 Non-constant sediment properties

Generally speaking, sediment data may have different particle size, sorting, porosity and relative density equivalence, and are not uniform. These characteristics lead to the increase of computational complexity (Adnan et al., 2019), so most of studies set the sediment parameters in the study area as a constant parameter for calculation (Mohd Salleh et al., 2024; Auguste et al., 2021). Actually, the spatial distribution of sediment parameters is not constant. Seabed sediment is not homogeneous, and as the distance from the shore increases, the grain size of the deposited sediment continuously decreases. Some researches had proved the validity of sand transport model with spatially variable sediment properties (Doroudi and

Sharafati, 2024; Bui and Bui, 2020). Sediment properties can be obtained by direct method and indirect method. The indirect method includes theoretical formula and empirical formula, while the direct method is sampling (Claude et al., 2012; Leary and Buscombe, 2020). Studies had shown that indirect methods are less effective than direct sampling (Claude et al., 2012). In this paper, sediment sampling is conducted using a clam grab sampler to collect surface geological samples from targeted sea areas. The study area is divided into river channel and estuary segments, with sediment samples collected at consistent intervals (Fig. 3). We sampled 15 points in estuary of the lower reaches of Changhua River and 40 points in the channel. To ascertain sediment parameters, including grain size and sorting factors, a laser particle size analyzer is utilized.

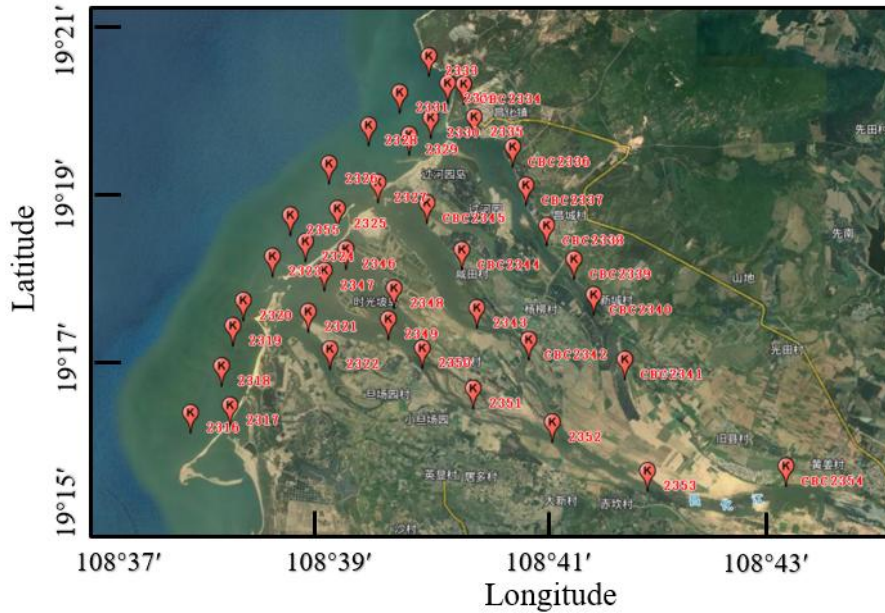


Figure 3: Location of sediment sampling point (map origination: <https://hainan.tianditu.gov.cn/>)

After selection, the analytical process detailed particle size and sediment segregation data (Table 2 and Table 3). Grain size parameters are quantitative representations of the grain size characteristics of the clastic material in terms of certain values. The individual grain size parameters and their combined characteristics can be used as the basis for discriminating the depositional hydrodynamic conditions and depositional environment. The commonly used parameters are mean particle diameter (Mz), sorting coefficient (δ_i) and median grain diameter (Φ_{50}). The number of samples at the estuary with a median grain diameter between 0 and 1ϕ is 9, accounting for 60 %; the number of samples with a mean grain size between 1ϕ and 3ϕ is 3, accounting for 20 %; the number of samples with a median grain size between -1ϕ and 0 is 3, accounting for 20 %. While, in the estuary and 40 points in the lower reaches, the number of samples with a median grain diameter between 0 and 1ϕ is 24, accounting for 60 %; the number of samples with a median grain size between 1ϕ and 3ϕ is 8, accounting for 20 %; the number of samples with a median grain size between 3ϕ and 7ϕ is 7, accounting for 17.5 %; the number of samples with a median grain size between -1ϕ and 0 is 1, accounting for 2.5 %.

Table 2 Grain parameters of samples at the estuary

Number	Coefficient of granularity			Classification of sediments
	Mean grain diameter Mz(ϕ)	Sorting factor δi	Median grain diameter $\Phi 50(\phi)$	
1	<0.04	0.7600	0.02	Gravel sand
2	<0.04	1.1000	-0.44	Sandy gravel
3	0.33	0.7600	0.33	Sand
4	<0.04	0.7900	0.01	Silty sand
5	0.50	0.7700	0.51	Sand
6	0.40	0.8200	0.41	Sand
7	0.98	0.6500	1.00	Sand
8	1.35	0.6900	1.41	Sand
9	2.91	0.9600	2.87	Sand
10	0.31	0.7700	0.32	Sand
11	0.26	0.7600	0.27	Sand
12	<0.04	0.6700	-0.41	Sandy gravel
13	<0.04	0.8000	-0.15	Silty sand
14	0.18	0.7700	0.19	Sand
15	0.70	1.2900	0.69	Sandy gravel

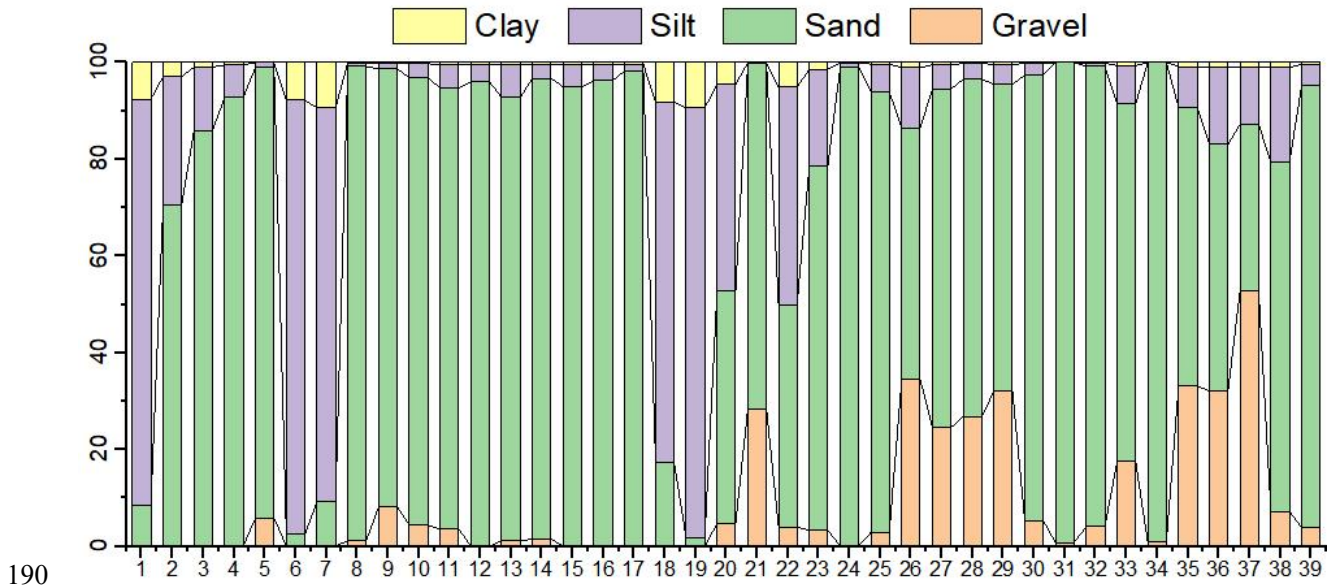
Table 3 Grain parameters of samples of the river

Number	Content of grain (%)				Coefficient of granularity			Classification of sediments
	Gravel	Sand	Silt	Clay	Mean grain diameter Mz(ϕ)	Sorting factor δi	Median grain diameter $\Phi 50(\phi)$	
1	0.00	8.55	83.90	7.55	6.01	1.42	6.09	Silt

2	0.00	70.64	26.48	2.88	3.33	2.14	2.44	Silty sand
3	0.00	85.98	13.06	0.96	2.82	1.26	2.79	Silty sand
4	0.00	87.44	6.38	0.45	2.64	1.27	2.57	Silty sand
5	5.90	93.12	0.98	0.00	0.15	0.75	0.16	Gravel sand
6	0.00	2.48	89.78	7.74	6.20	1.26	6.22	Silt
7	0.00	9.12	81.51	9.37	6.25	1.47	6.45	Silt
8	10.96	87.75	0.97	0.07	<0.04	0.70	-0.17	Gravel sand
9	1.18	98.02	0.75	0.05	0.51	0.72	0.52	Gravelly sand
10	8.18	90.50	1.21	0.11	0.12	0.84	0.11	Gravel sand
11	4.42	92.40	2.95	0.23	0.30	0.83	0.29	Gravelly sand
12	3.56	91.40	4.77	0.46	0.79	1.33	0.74	Gravelly sand
13	0.03	96.04	3.57	0.36	1.17	0.86	1.17	Gravelly sand
14	1.13	91.58	6.84	0.45	1.24	1.40	1.16	Gravelly sand
15	1.51	95.25	2.90	0.33	0.71	0.92	0.68	Gravelly sand
16	0.00	94.96	4.68	0.35	1.32	1.00	1.31	Sand
17	0.00	96.21	3.47	0.32	1.34	0.81	1.33	Sand
18	0.00	98.26	1.40	0.34	1.21	0.71	1.20	Sand
19	0.00	17.37	74.44	8.20	5.89	1.81	6.33	Sandy silt
20	0.00	1.61	89.02	9.37	6.33	1.27	6.39	Silt
21	4.70	47.88	42.65	4.52	3.43	3.20	3.69	Gravelly muddy sand
22	28.43	71.40	0.12	0.05	0.69	0.84	0.75	Gravel sand
23	4.01	45.93	44.98	5.07	3.57	3.19	3.99	Gravelly mud
24	3.26	75.71	20.00	1.42	1.77	2.53	0.63	Gravelly muddy sand
25	0.05	98.99	0.88	0.08	0.91	0.70	0.92	Gravelly sand
26	2.86	91.07	5.73	0.34	0.67	1.29	0.62	Gravelly sand
27	40.14	60.58	14.52	1.16	1.54	2.66	0.39	Muddy sandy gravel
28	24.57	69.98	4.97	0.47	0.13	1.43	0.11	Gravel sand
29	26.79	69.74	3.26	0.21	0.56	0.99	0.55	Gravel sand
30	36.45	72.08	4.72	0.40	0.21	1.35	0.22	Sandy gravel

31	5.23	92.23	2.34	0.20	0.30	0.83	0.30	Gravel sand
32	0.79	99.21	0.00	0.00	0.73	0.75	0.75	Gravelly sand
33	4.06	95.54	0.68	0.08	0.44	0.82	0.47	Gravelly sand
34	17.53	73.84	8.00	0.63	0.36	1.59	0.29	Gravelly muddy sand
35	0.85	99.15	0.00	0.00	0.64	0.72	0.65	Gravelly sand
36	38.74	67.26	9.86	0.98	0.58	1.82	0.33	Muddy sandy gravel
37	32.10	51.01	15.89	1.01	1.61	2.73	0.26	Muddy sandy gravel
38	52.91	34.33	11.76	1.01	1.64	2.91	0.07	Muddy sandy gravel
39	7.23	72.16	19.53	1.07	1.46	2.53	0.38	Gravelly muddy sand
40	3.81	90.24	4.21	0.37	0.38	0.94	0.45	Gravelly sand

185 The surface sediment particles in the nearshore area of Changhua river course are mainly divided into three grain size components, gravel (>2 mm), sand (0.063~2 mm), silt (0.004~0.063 mm), with relative percentages of 9.28%, 72.18% and 18.54%, respectively. Based on the sampling and testing results of the river course, we can obtain the histogram of the component percentage for each sample (Fig. 4). It is obvious that the sediment composition in the river channel is dominated by sand, followed by silt.



190 **Figure 4: Percentage composition of components in river samples**

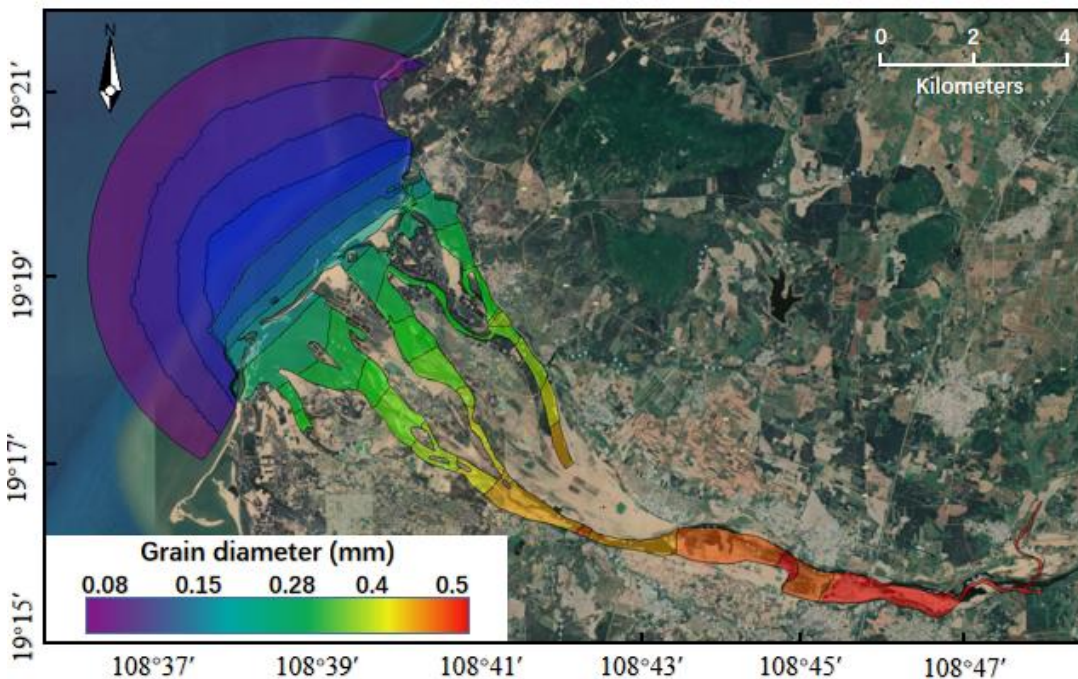
According to the classification criteria of the sorting coefficients by Focke–Ward (Table 4), Sediments from the Changhua River estuary in the lower reaches exhibit medium sorting with coefficients of most samples between 0.71~1.00 and a median grain diameter predominantly under 1.5 mm, characterized mainly by sand. In contrast, sediments within the river

195 stretch between Baoqiao Station and the lower reaches are coarser with poorer sorting, evidenced by a sorting coefficient exceeding 1.00 in 23 out of 40 samples (over 57 %).

Table 4 Sorting level table

Sorting Grade	Sorting factor (δ_i)
Sorting excellent	<0.35
Sorting good	0.35~0.71
Sorting medium	0.71~1.00
Sorting poor	1.00~4.00

To ascertain the sediment composition and the dry bulk density in the estuary, 15 samples were collected from the Changhua River estuary. These samples were dried to measure mass and volume, thereby determining the dry bulk density of the sediment. After calculating, the dry bulk density is 1210.9 kg/m³ which used in sand transport model. This analysis is crucial for model accuracy and understanding sediment behavior in the estuarine environment. According to the sampling position, the research area is divided into areas. After sorting and interpolation, the spatial variation of sediment particle size data and sorting data in the study area are obtained (Fig. 5).



205 **Figure 5: Variation of sediment particle size data (map origination: <https://hainan.tianditu.gov.cn/>)**

2.4 Reliability evaluation index

In this paper, Nash-Sutcliffe model efficiency coefficient (NSE) and root mean squared error (RMSE) are used to evaluate the reliability of the model. The calculation formulas (Nash and Sutcliffe, 1970) are as follows:

$$NSE = 1 - \frac{\sum_{i=1}^N (M_i - O_i)^2}{\sum_{i=1}^N (O_i - \bar{O})^2} \quad (14)$$

$$RMSE = \sqrt{\frac{\sum_{i=1}^N (M_i - O_i)^2}{N}} \quad (15)$$

In Equations: M_i is the model simulation value at the i moment; O_i is the measured value at the i moment; \bar{O} is the average of the measured values of the site at all simulation moments; N is the total number of all simulation moments. Among them, the value range of NSE is 0~1. When $0.65 \leq NSE < 1$, the fitting degree of the model is excellent; When $0.5 \leq NSE < 0.65$, the fitting degree of the model is good; When $0.2 \leq NSE < 0.5$, the fitting degree of the model is general; When $0 < NSE < 0.2$, the fitting degree of the model is poor.

3 Model Region and Settings

The study area is situated in the western part of Hainan Island, mainly encompassing the lower reaches of Changhua River and its estuary. The approximate coordinates range from 108 36'E to 108 50'E and 19 15'N to 19 22'N. The study area covers a large part of the region from Chahe Town to the estuary of the Changhua River, including towns such as Changhua Town, Sigeng Town, Sanjia Town, and Wulie Town, among others. An unstructured grid, finite volume, regional ocean model FVCOM (Chen et al., 2003) was used to simulate the hydrodynamic background and hydrological features. It has been widely used for the study of coastal oceanic and estuarine circulation (Jiang and Xia, 2016; Huang et al., 2008; Lai et al., 2018; Chen et al., 2008). The model's open boundary relies on forced tidal level data extracted using the Earth and Space Research's (ESR) Matlab "Tide Model Driver" (TMD) toolbox (<https://www.esr.org/research/polar-tide-models/tmd-software/>) from the TPXO 6.2 global tidal wave prediction model.

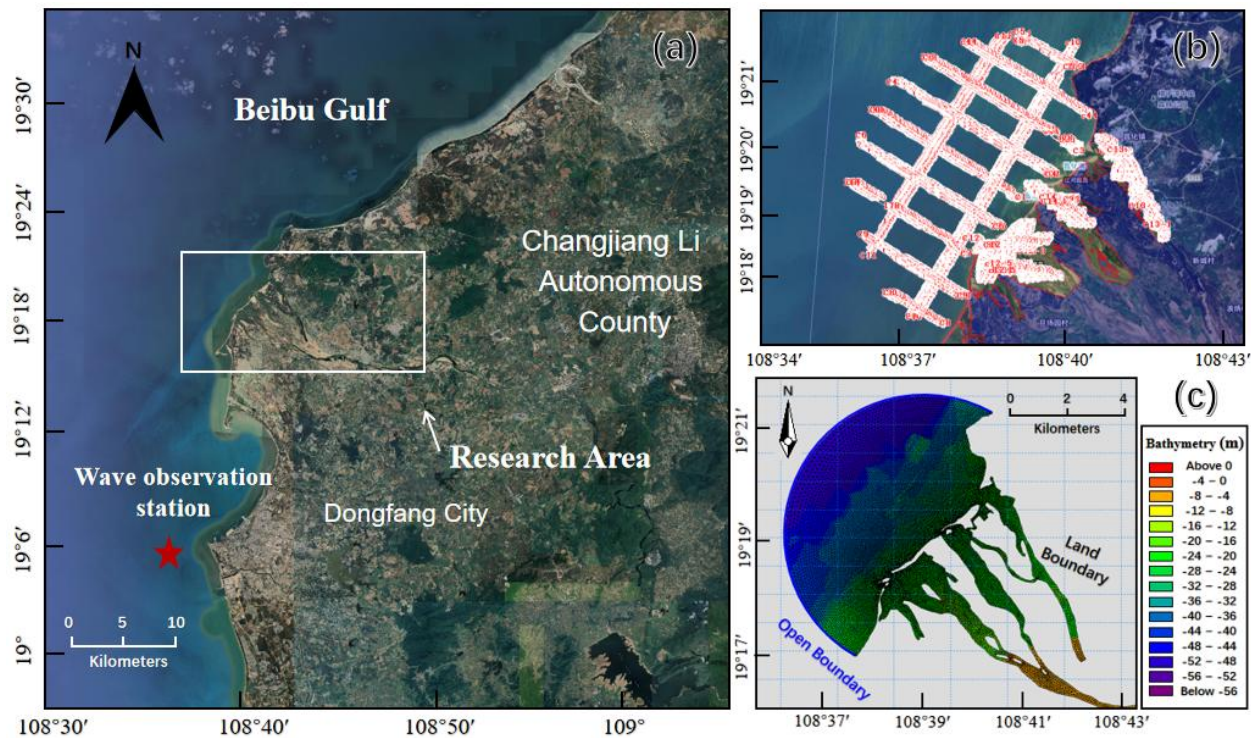


Figure 6: (a) Scope of study area (the white frame) and wave observation (the red star) from Dongfang; (b) ADCP collection points on site; (c) Grids and boundaries (map origination: <https://hainan.tianditu.gov.cn/>)

In the study, bathymetric data is derived from ETOPO1 global seafloor topography data and in-situ measurements using ADCP. The spatial resolution of ETOPO1 data is $1/60^\circ \times 1/60^\circ$, which is insufficient for the research requirements. ADCP depth measurements have higher density in nearshore areas and provide actual measured data with higher accuracy. The model employs a triangular unstructured grid. To enhance computational accuracy and reduce computation time, the density of boundary nodes gradually decreases from nearshore to offshore. In the offshore region, the grid density is lower, with a resolution of 0.25 km, while the nearshore part of the open boundary has higher grid resolution. In the main research area near the river channel, the grid resolution is highest, reaching 25 m. The entire study area grid comprises a total of 13, 814 computational nodes. The wave parameters at the open boundary are set to fixed values, referring to the annual average frequency of occurrence of wave heights in various directions at the Dongfang Ocean Station over the years (Ding, 1990; Hu, 2009; Wang, 2023).

The model's open boundary conditions are defined by the forced tidal water level, incorporating eight primary tidal components: M2, S2, K1, O1, N2, K2, P1, and Q1. The model's closed boundary aligns with the terrestrial boundary, where the normal velocity of ocean currents is set to zero, precluding any exchange of temperature and salt between land and seawater. The time resolution of tidal level data is 1 hour and the accuracy is 1 cm. There are 121 open boundary control points. The model also integrates the impact of wind fields, with data sourced from ECMWF at a resolution of $1/8^\circ \times 1/8^\circ$.

This dataset encompasses the u (east-west) and v (north-south) components of the wind vector, along with sea level pressure. The upper boundary of the model is set based on the multi-year average monthly flow and sediment concentration data from the Baoqiao Hydrological Station in Chahe Town. The upstream boundary is assigned a flow rate of 44 m³/s, and the suspended sediment concentration is set at 5 g/m³. The median grain size and sorting coefficient of the initial sediment distribution are determined through the partitioning based on the measured sediment data from Section 2.3. The porosity is set to 0.4, and the sediment density is 2650 kg/m³. In this study, we calibrated the hydrodynamic model using water level data from April and May of 2022. The data were collected from Basuo port station. One-At-a-Time (OAT/OFAT) method (Czitrom, 1999) is used to modify the parameters, an effective local sensitivity analysis technique. In each experiment, we alter one factors while holding the others constant. During the calibration process, our primary focus was on the model's hydrodynamic response. This was achieved by adjusting the flow resistance parameters and the bed roughness coefficients within the model. The calibrated model parameters are presented in Table 5.

Table 5 Parameters of the hydrodynamic model

Parameter	Value
Shoreline	GSHHS
Bathymetry	ETOPO1 and ADCP in-situ
Grid	0.25 km at the boundaries to 25 m near the coastline
Time period	23/4/2023 00:00-30/4/2023 00:00 (Spring neap tide) 28/6/2022 00:00-1/8/2022 00:00 (High water period)
Manning number	28
Eddy viscosity	Smagorinsky formulation data 0.28 m ² /s
Time step	300 s
Tidal constituents	M2, S2, K1, O1, N2, K2, P1, Q1
Wind/Sea level Pressure	ERA 5
Validation	Basuo Port Station (19°06' N, 108°37' E) ADCP 01, ADCP 02

Considering the limitations of the FVCOM model in wave calculations, this study selects the widely-used third-generation SWAN model (SWAN team, 2006) for numerical simulation of wind waves in this region. The wave field are driven by wind and current from hydrodynamic model. The parameters used in the model setups are based on the values listed in Table 6. The wave model at the open boundary is defined by the JONSWAP spectrum, with a spectral resolution of 40 frequency bins and 36 directional sectors. The directional resolution is set to 40 sectors. Calibrate the parameters using multi-year wave data from the Dongfang Ocean Station. The wind speed and wind direction are from the ERA5 reanalysis data provided by

ECMWF. The peak parameter (γ) of the JONSWAP spectrum, indicative of the wave asymmetry, was specified at 3.3, and the spectral width parameter was set to 0.07 to define the shape of the wave spectrum.

Table 6 Parameters of the wave model

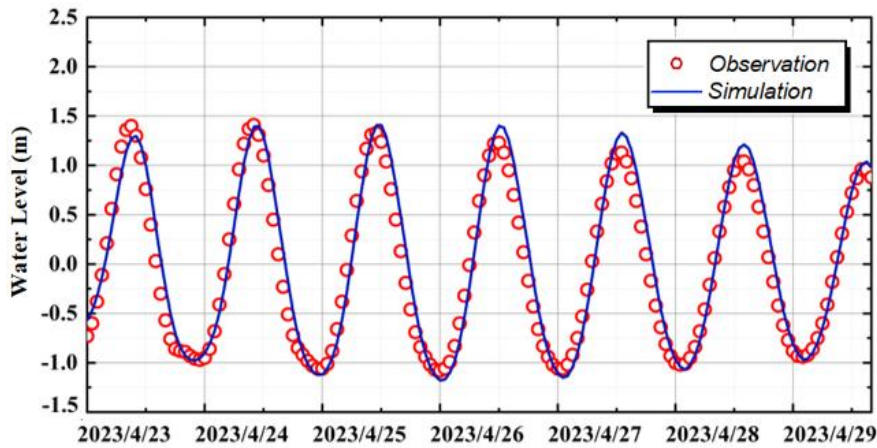
Parameter	Value
Whitecapping dissipation (C_{ds})	2.36×10^{-5}
Pierson–Moskowitz (S_{pm})	3.02×10^{-5}
Dissipation (alpha)	1.0
Breaking index (gamma)	0.73
JONSWAP formulation (C_{bottom})	0.067

265 A mathematical model established through a wave-current coupling approach can accurately describe the motion laws of
 wave-generated currents and consider the impact of nearshore currents on wave propagation. It also reflects the interaction
 between nearshore waves and currents. In this paper, a three-dimensional sediment transport model is constructed using the
 model coupler MCT to perform real-time coupling between the hydrodynamic model FVCOM and the wave model SWAN,
 employing the same unstructured grid for the coupling (Chen et al., 2018; Ji et al., 2022). The coupling process can be
 270 summarized as follows: the FVCOM hydrodynamic model and the SWAN wave model transmit the calculated three-
 dimensional flow field and wave data to the sediment module, which then calculates the suspended and bed load sediment
 transport rates, achieving data linkage between the three-dimensional wave-current coupled model and the sediment
 transport model.

4 Hydrodynamic Model

275 4.1 Verification of hydrodynamic model

In order to ensure the validity of the model, the tidal current data of one tide gauge station and two ADCP points in the study
 area are compared and verified. Figure 7 shows the hourly water level comparison between the measured tidal water level at
 Basuo Port Station (19°06'N, 108°37'E) and the model simulation results. Model validation occurs from 10:00 on April 23,
 2023, to 00:00 on April 30, 2023. After calculation, the RMSE of the simulation results is 18.101 cm and the NSE is 0.9501,
 280 which is within the acceptable range. This shows that the model is reliable and meets the demand, and can be used to
 simulate the tidal current in the research area of the lower reaches of Changhua River.



Name:
Basuo Port Station

Position:
108°37' E, 19°06' N

Duration	Reliability index	
	NSE	RMSE
6 day	0.9501	18.101 cm

Figure 7: Hourly water level verification of Basuo Port Station

285 During the sea trial, two points were selected to continuously observe the velocity and direction of seawater. In order to obtain the seawater situation in lunar day, the continuous measurement time of each point was 25 hours. Information about the position and observation time of the measuring point is as follows (Table 7 and Fig. 8).

Table 7 Information of fixed-point current station

Number	Position	Observation
ADCP 01	108°37'28''E, 19°18'10''N	April 23rd at 10: 00 - April 24th at 11: 00
ADCP 02	108°39'21''E, 19°20'55''N	April 24th at 17: 00 - April 25th at 18: 00

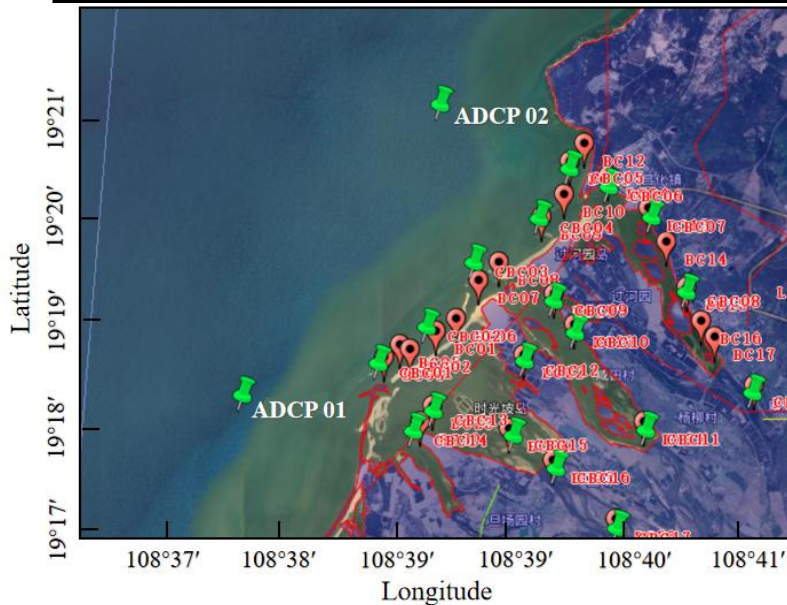


Figure 8: Specific location of ADCP

290 Current velocity and direction verification at the Changhua River estuary involves a 5-minute time resolution analysis using an Acoustic Doppler Current Profiler (ADCP). Located over 2 km offshore with a water depth of 20.9 m, ADCP 01's data is compared against simulations at five-minute intervals. The 25-hour observation period, from 10:00 on April 23, 2023 to 11:00 on April 24, 2023, encompasses a full lunar day, providing a comprehensive dataset.

The model's simulated velocity and direction are found to be in substantial agreement with the ADCP 01 measurements, particularly in regions where tidal currents are predominant. The model accurately replicates the velocity fluctuations, affirming its capability to capture the dynamics of the study area. The proximity of measurement point ADCP 01 to the land, coupled with its relatively shallow water depth, results in sea water being more susceptible to obstruction by the topography and friction from the seafloor at this location. This results in a reduced error, validating the model's performance. The consistency between the model and the measurements confirms the high reliability of the model for future research applications.

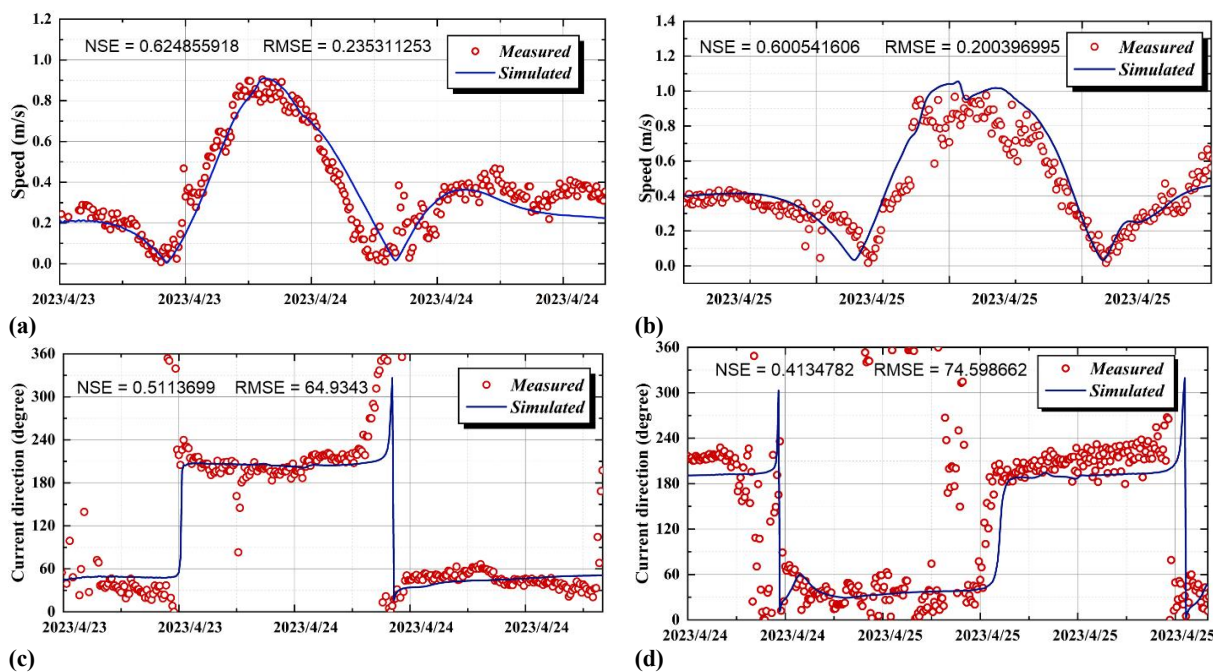
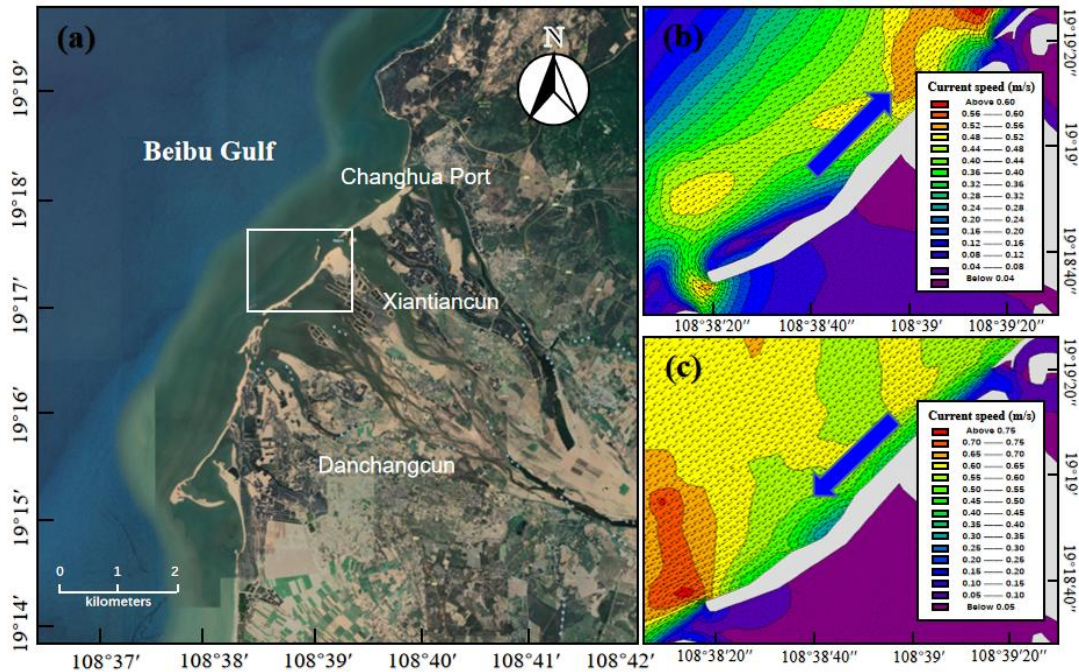


Figure 9: Current velocity and direction verification. (a) velocity verification of ADCP 01; (b) velocity verification of ADCP 02; (c) verification of current direction of ADCP 01; (d) verification of current direction of ADCP 02

4.2 Results of hydrodynamic model

The hydrodynamic simulation outcomes, as depicted in Fig. 10, indicate a predominantly NE-SW reciprocating current pattern within the study area. This flow is aligned parallel to the coastline, with the tidal current shifting direction according to the tidal phase. Figure 10b and 10c depict the flow field outside the estuary of the Changhua River. Figure 10b shows the flow field at 23:00 on April 23, 2023, corresponding to the peak of the flood tide. At this time, the tidal current flows in a northeast direction with a maximum speed of 0.62 m/s. Figure 10c shows the flow field at 13:30 on April 24, 2023,

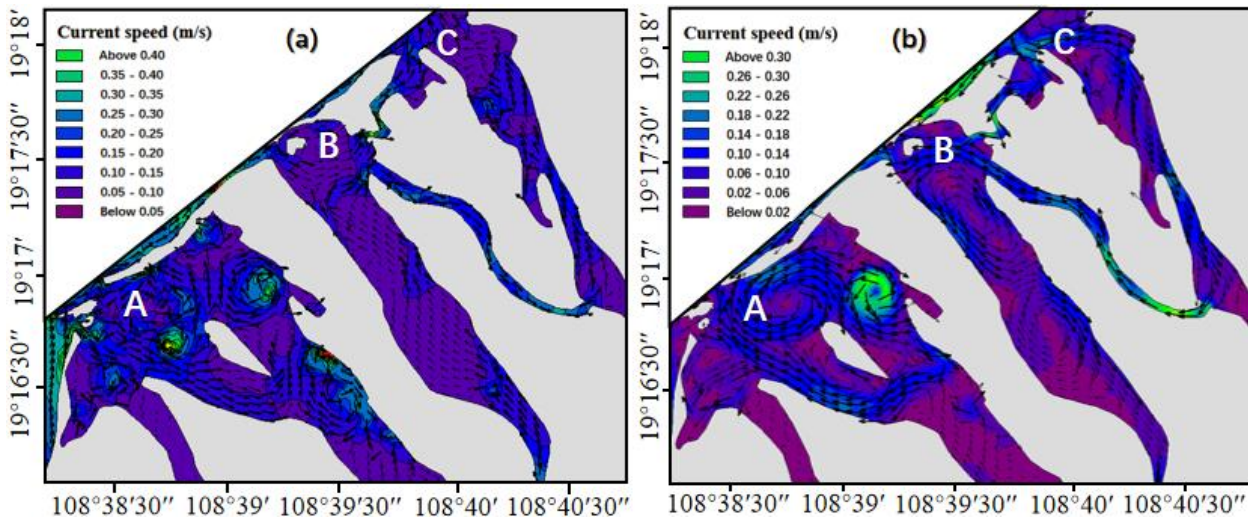
310 corresponding to the peak of the ebb tide, where the tidal current flows in a southwest direction with a maximum speed of 0.75 m/s. Overall, the tidal currents outside the Changhua River estuary generally follow a northeast-southwest reciprocating pattern, with flood tides flowing northeast and ebb tides flowing southwest, parallel to the shoreline. The maximum ebb current is faster than the maximum flood current.



315 **Figure 10: Study area and coastal current direction. (a) location map of the study area; (b) detailed zoom of the map in Fig. 10a with NE current; (c) detailed zoom of the map in Fig. 10a with SW current. (map origination: <https://hainan.tianditu.gov.cn/>)**

320 Figures 11a and 11b illustrate the flow field inside the estuary of the Changhua River. Figure 11a shows the flow field at 23:00 on April 23, 2023, corresponding to the peak of the flood tide. Inside Estuary A, due to the topography, a large counterclockwise circulation forms around the central island, accompanied by several smaller vortices, with the overall trend of tidal currents flowing southeast along the river channel. In Estuary B, ocean inflows meet with river flows from upstream, ultimately converging into Estuary C through the passage between B and C. In Estuary C, the flow is more unidirectional compared to A and B, with upstream water flowing into the ocean, then following the northeast-directed tidal current outside the Changhua River estuary. Figure 11b shows the flow field at 13:30 on April 24, 2023, at the peak of the ebb tide. At this time, the circulation inside Estuary A reverses to a clockwise direction, and other smaller vortices change direction accordingly, with the overall trend of tidal currents flowing from upstream to the ocean. In Estuary B, the dominant force is the high-speed flow from Estuary C, which enters B through the narrow passage between B and C, splitting into two opposite directions: one part flows into the ocean, and the other flows upstream, forming a circulation within the river channel. In Estuary C, the water flows upstream from the ocean along the river channel.

325



330 **Figure 11: Flow field inside the estuary. (a) moment of the maximum flood current; (b) moment of the maximum ebb current**

To further analyze the characteristics of the flow field in the study area, flow fields are selected for analysis during the transition from low tide to high tide and from high tide to low tide. Figure 12f depicts the location of the research area. Figure 12a shows the flow field at low tide, where the tidal current outside the estuary flows northeast, and water in the main river channel downstream of the Changhua River flows upstream from the ocean. After low tide (during flood tide), water
 335 flow velocity gradually increases, with the tidal current outside the estuary consistently flowing northeast. During this period, the main river channel maintains an eastward flow.

Figure 12b illustrates the moment of flow direction change during flood tide, when the flow direction outside the estuary rotates clockwise along the shoreline from the south (toward Beili Bay). The northern ocean current (outside Changhua Harbor) also begins to rotate clockwise, flowing into Estuary C, then into the ocean through the passage between B and C,
 340 forming a circulation that enhances the clockwise rotation of the northern ocean current. Subsequently, the flow direction gradually changes from northeast to southwest as it moves from the coast toward the open sea. The sand spit at the downstream estuary alters the flow direction and velocity. The sand spit can act as a natural barrier, causing the tidal current to change direction earlier during flood tide.

Figure 12c shows the flow field at high tide, where the tidal current outside the estuary has fully shifted to the southwest, while the flow direction further offshore is still transitioning. In the main river channel, the water flows from upstream toward the ocean. Estuaries B and C are influenced by the coastal current outside the northern part of the study area, flowing into the estuary opposite to Estuary A. After high tide (during ebb tide), the water flow velocity in the study area gradually increases, with the tidal current outside the estuary consistently flowing southwest. After some time, the water currents in the southern and northern parts of the study area turn counterclockwise, and the flow direction in the B and C channels changes
 345 from inward to outward.
 350 from inward to outward.

Figure 12d shows the flow field at the moment when the flow direction changes during ebb tide. It is evident that there are two counterclockwise circulations outside the Changhua River estuary: one from Beili Bay and the other from outside Changhua Harbor. The latter has a broader influence and thus plays a dominant role in determining the water flow direction in the study area, gradually shifting the coastal current from southwest to northeast. Figure 12e shows the flow field at low tide once again, where the water flow outside the estuary has shifted back to the northeast, repeating the previous flow pattern.

In summary, during the transition from flood to ebb tide, the flow field outside the estuary is driven by the deflection of water currents from Beili Bay and Changhua Port, shifting the flow direction from northeast to southwest. During the transition from ebb to flood tide, the deflection is primarily influenced by the circulation outside Changhua Port, shifting the flow direction from southwest to northeast. In channels A, B, and C within the study area, the flow direction changes are relatively consistent due to the passage between B and C. The flow direction in channel A aligns with the main river channel, flowing inward during flood tide and outward toward the ocean during ebb tide.

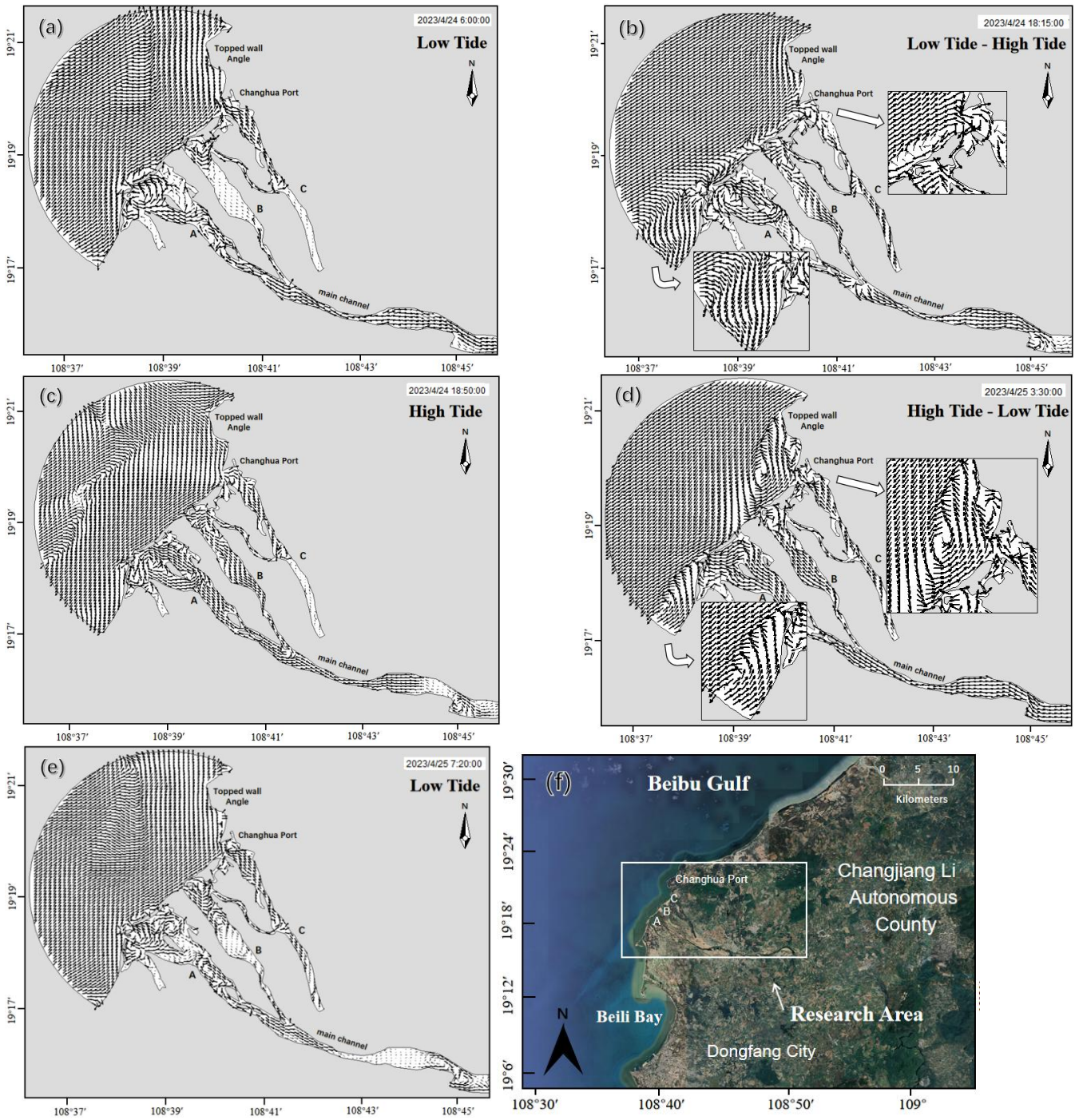


Figure 12: Transition of the flow field (a-e) and location of the study area (f)

5 Sand Transport Model

5.1 Verification by suspended sediment concentration

In the lower reaches of the Changhua River, the summer season is the most pronounced for sediment variation within a year, with the highest sediment concentration and sediment transport rate (Mao et al., 2006). Therefore, sediment data from July, which is representative, are selected for model validation. The simulated Suspended Sediment Concentration (SSC) is compared with the daily observed SSC at Baoqiao Station for the month of July (Fig. 13). The SSC at Baoqiao Station is the highest during the first two days of July, reaching a peak SSC of 0.55 kg/m^3 . Subsequently, the SSC continuously decreases, reaching its lowest value on the 5th of July, and then slowly rises. After the 10th of July, it gradually decreases from 0.301 kg/m^3 , with the most values remaining below 0.2 kg/m^3 . Based on the analysis, NSE for Baoqiao Station is 0.8389; the RMSE is 0.097244 kg/m^3 . The observed SSC are in good agreement with the simulated values.

To further analyze the simulation validation, Fig. 13 presents a histogram of the daily absolute error in SSC at Baoqiao Station. The absolute error is calculated as the absolute difference between the measured and simulated values. The Mean Absolute Error (MAE) is defined as the average over the test sample of the absolute differences between prediction and actual observation. The MAE in SSC for Baoqiao Station in July is 0.071224 kg/m^3 . The maximum error occurs at the beginning and the end of the month, which may be due to the use of monthly average flow and sediment data for the model's upper boundary input, thereby increasing the model's error. Overall, the difference between the daily observed SSC values and the simulated results at Baoqiao Station in July is within a reasonable range, indicating that the model has an acceptable level of precision.

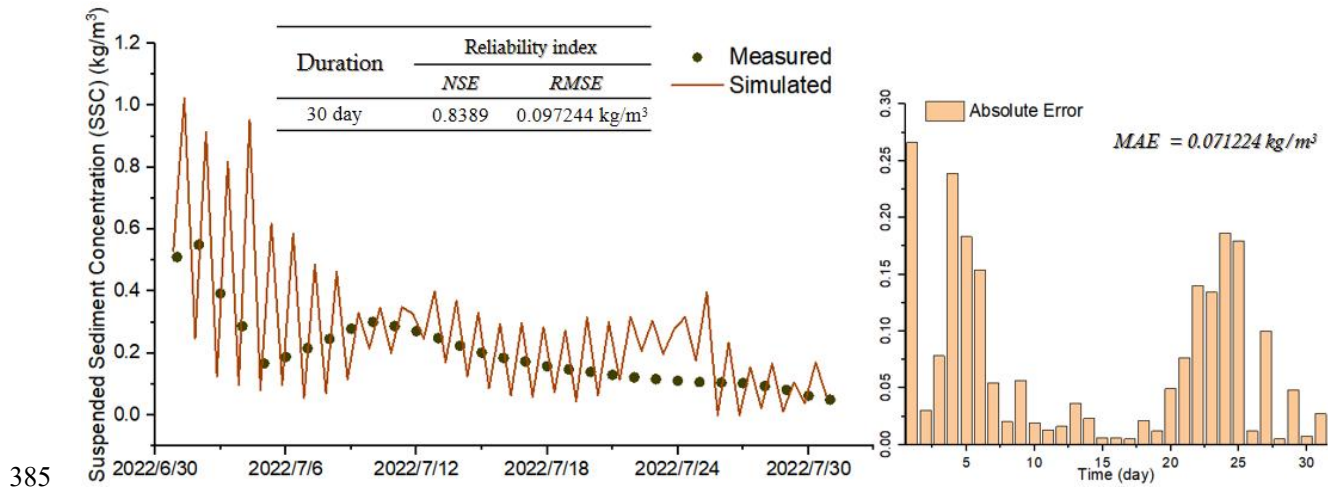


Figure 13: Selection point for sediment deposition verification

5.2 Analysis of depositions in Changhua River estuary

Sediment deposition in the Changhua River estuary is influenced by both hydrodynamic and geological factors. The predominant northeast-southwest tidal current direction and wave action, has led to the formation of a two-way sand mouth, further narrowing the estuary. Secondly, the estuary's geomorphology consists of a sandy riverbed with poor stability. The bed slope at the estuary decreases, and the water flow's capacity to carry sediment is reduced. Therefore, the sediment accumulation at the mouth of the Changhua River is relatively severe..

Over time, these processes have resulted in the formation of two river islands, altering the estuary into a complex channel system with multiple smaller estuaries. Currently, the main river channel flows between these islands, exhibiting shallow depths during low tide. These findings are pivotal for understanding the estuary's morphological evolution and inform strategies for sediment management in such dynamic environments.

There are two obvious depositions in the study area, including the estuary and the slender channel. The figure clearly shows the serious and slight areas of siltation in the study area. However, the specific sedimentary characteristic in the study area is unknown, needing further analysis. To solve this problem, we extract the bed level change data of a point in the obvious change area of river bed, and take this point as the whole area. Therefore, the sediment deposition characteristic in this area can be analyzed through the bed level change at this point.

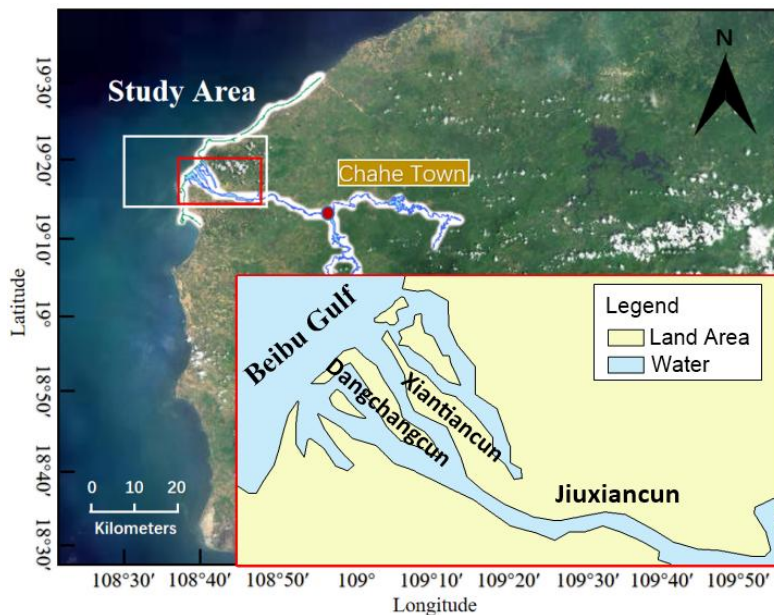


Figure 14: Information of important place names in simulated areas

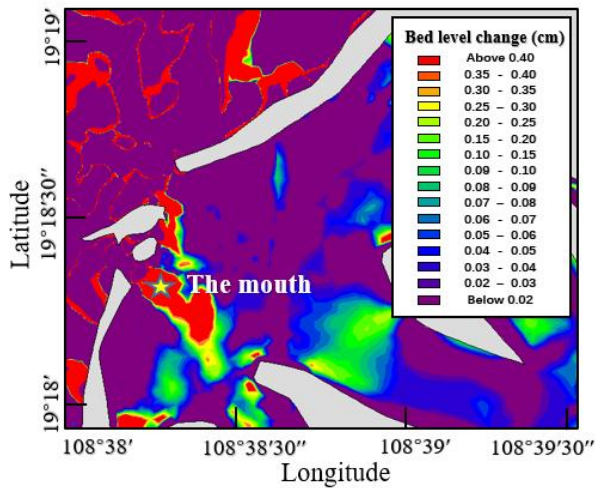
Results of Danchangcun are shown in Fig. 15, which illustrates the bed level changes and consequent sediment deposition and scouring in various parts of Danchangcun. Positive values indicate sediment deposition, while negative values denote scouring.

In the estuary of Danchangcun (Fig. 15b), the bed level fluctuates above zero, signifying net sediment deposition with a final accumulation of approximately 0.59 cm over the simulation period.

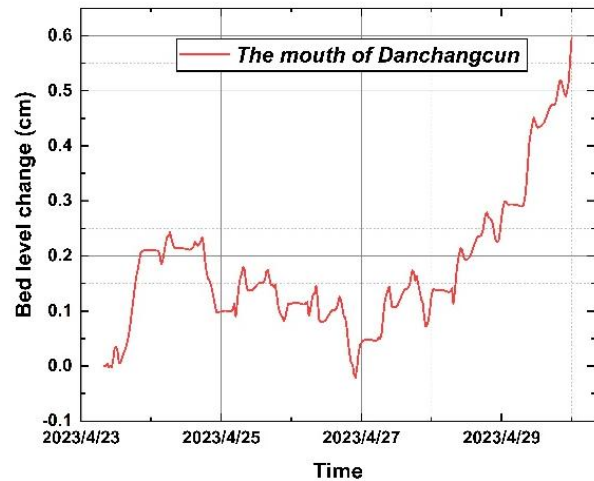
410 The deposition near the river island in Danchangcun (Fig. 15d) follows a cyclical pattern over a 24-hour cycle, with an overall sediment thickness of about 0.20 cm. Initially, sediment accumulates quickly, after which the bed level stabilizes at its peak value. A sharp decrease in deposition rate is observed in the last two hours, with each cycle adding about 0.03 cm of sediment.

415 At the front end of the sand mouth (Fig. 15f), the bed level decreases by 0.39 cm, indicating active scouring and sediment removal. The continuous negative bed level changes suggest an increasing scouring intensity, especially pronounced on April 23 when a significant erosion event led to a 0.18 cm drop in bed level.

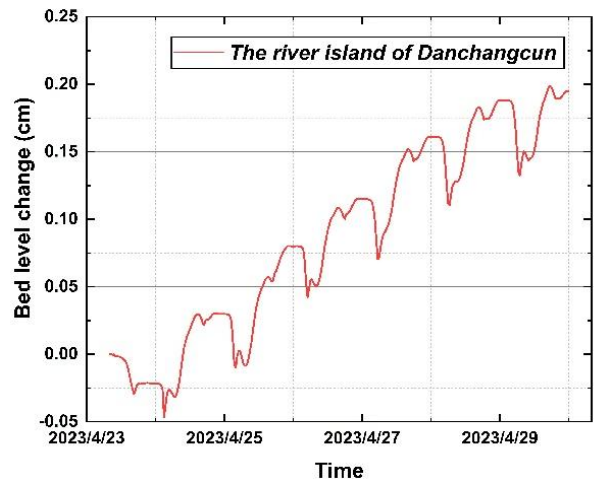
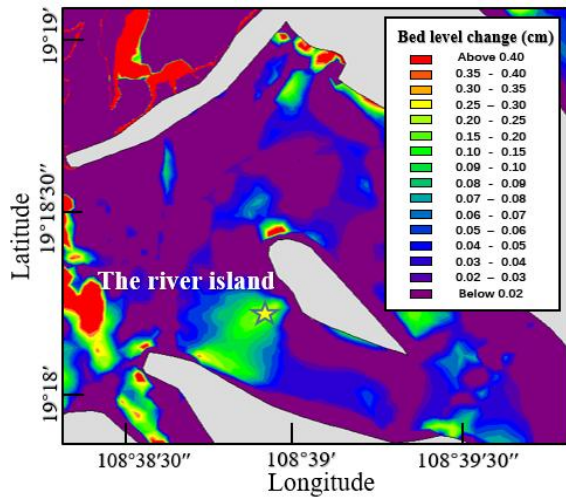
420 Finally, Figure 14h examines sediment deposition at the sand mouth, with two distinct locations showing similar sedimentation trends, albeit with Location 2 (near the river) experiencing faster sedimentation. Prior to April 24-25, Location 1 (near the ocean) registered erosion, followed by a transition to net deposition, while Location 2 showed minor erosion before April 24. The simulation predicts final bed level changes of approximately 0.42 cm for Location 1 and 0.60 cm for Location 2.



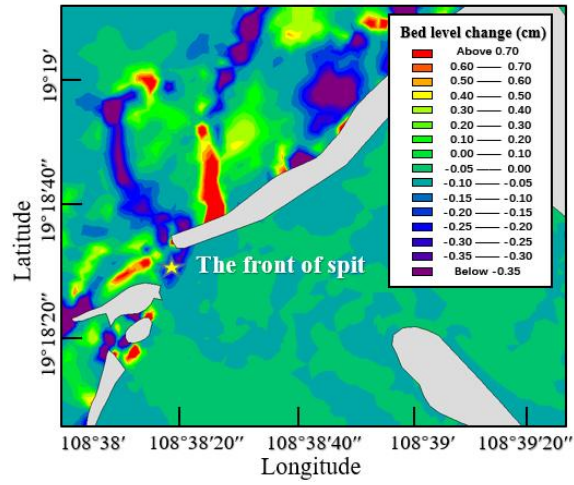
(a)



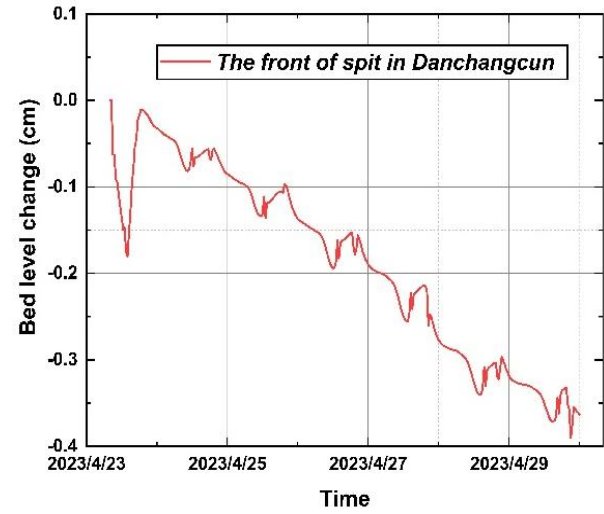
(b)



(c)

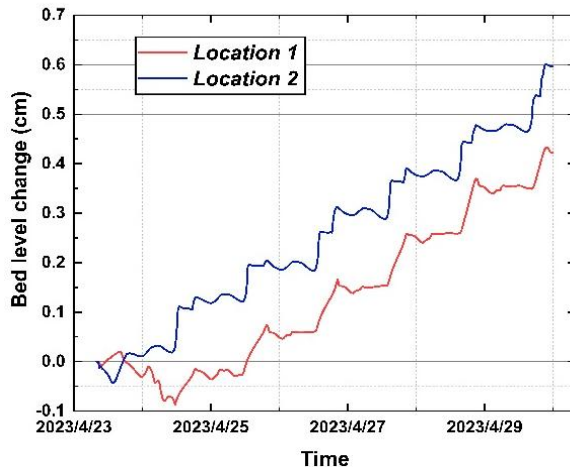
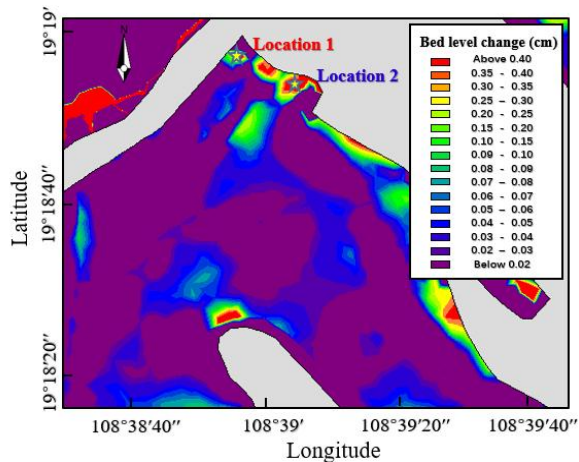


(d)



(e)

(f)



(g) **Figure 15: Bed level change of deposition in Danchangcun**

From April 27th to 30th, an overall increase in deposition thickness was noted, reaching approximately 0.59 cm. Two rapid deposition phases were identified: the first, on April 23rd from 13:30 to 20:30, coincided with astronomical mid-tide but exhibited lower current velocities than expected, as per ADCP 01 measurements. The second phase followed an spring tide on April 22nd, which stirred turbulent currents and enhanced scouring, leading to increased sediment concentration in the estuary. The tide on April 23rd was moderate, significantly reducing current velocity and sediment transport capacity, resulting in sediment deposition in the estuary.

On April 27th, during astronomical neap tide, lower water levels and reduced tidal ranges led to slower currents, enhancing sedimentation and weakening lateral erosion. The current's reduced capacity limited the transport of larger sediment particles, allowing only fine grains to settle at the water's bottom. These findings underscore the complex interplay between sediment deposition and erosion in estuarine environments and highlight the influence of tidal dynamics on sediment transport processes.

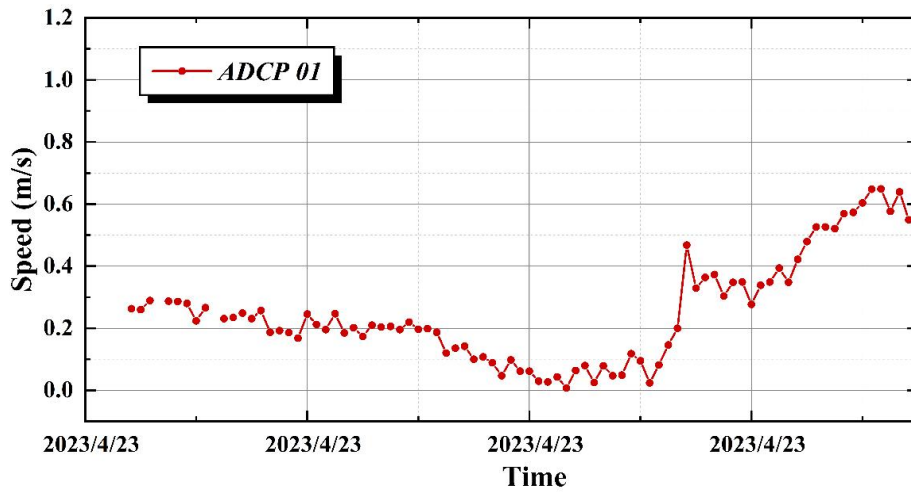
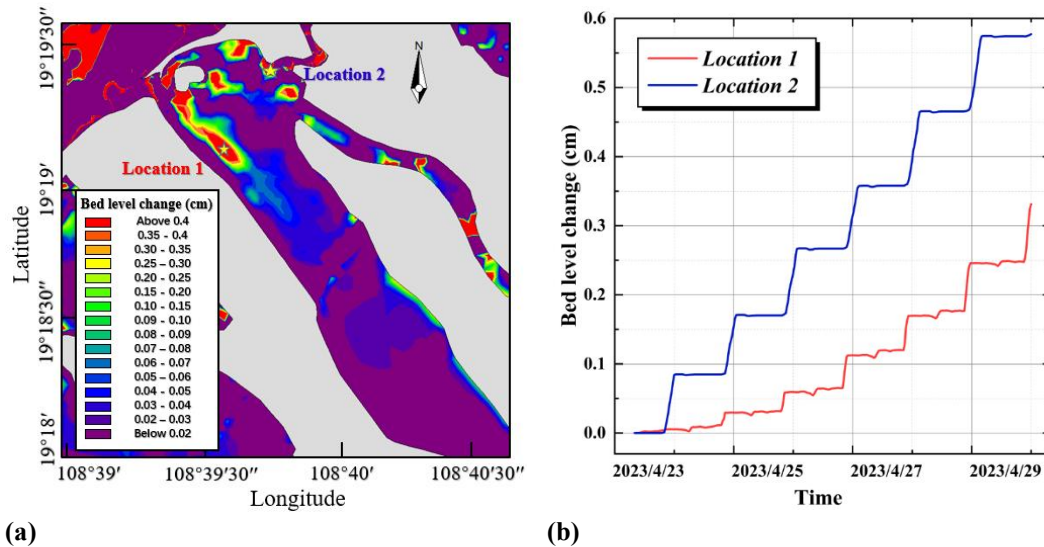


Figure 16: Current speed on April 23rd

435 In the Xiantiancun estuary, sediment deposition is influenced by its narrower configuration compared to Danchangcun, with numerous tributaries contributing to a dispersed flow and reduced kinetic energy. This results in variable sediment deposition levels at the entrances of the tributaries, although the overall deposition is less extensive than at the Danchangcun mouth. The maximum observed deposition thickness within the estuary is 0.58 cm at Location 2, while other areas exhibit thicknesses between 0.3 cm and 0.5 cm.

440 Two significant deposition sites are located near the sand mouth, which may facilitate the mouth's further expansion. Additionally, a substantial, albeit thin, silting zone is identified at the rear of the river island (Location 1), covering a considerable area. These findings indicate the complex interplay of sedimentary processes in estuarine environments and the potential for morphological changes due to deposition patterns.



445 **Figure 17: Deposition in Xiantiancun: (a) shows changes of sedimentation thickness of Xiantiancun with palette; (b) shows changes of sedimentation thickness of Xiantiancun in detail.**

To summarise, the Changhua River estuary exhibits distinct sedimentation patterns, with notable deposition occurring in both the estuary and slender channel regions. The estuary depositions are a result of interplay between hydrodynamic conditions and geological settings. Specifically, the estuary is subject to persistent northeast-southwest coastal currents and wave action, leading to the formation of a two-way sand mouth that constricts the estuary's width. The sandy, unstable riverbed further contributes to substantial sediment deposition due to the reduced gradient and sediment transport capacity of the fluctuating discharge. This has, over time, led to the formation of river islands, transforming the estuary into a complex channel system with multiple small estuaries. The main channel, situated between these islands, experiences shallow water depths during low tide.

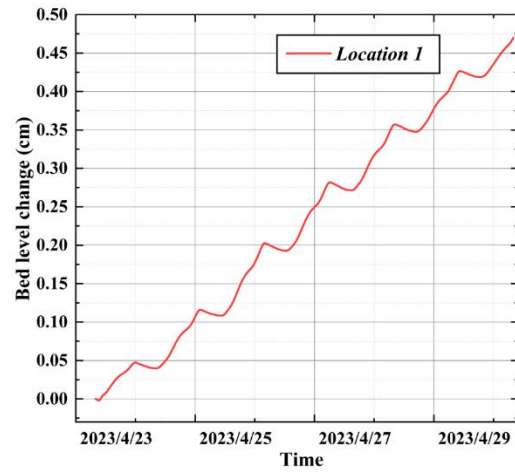
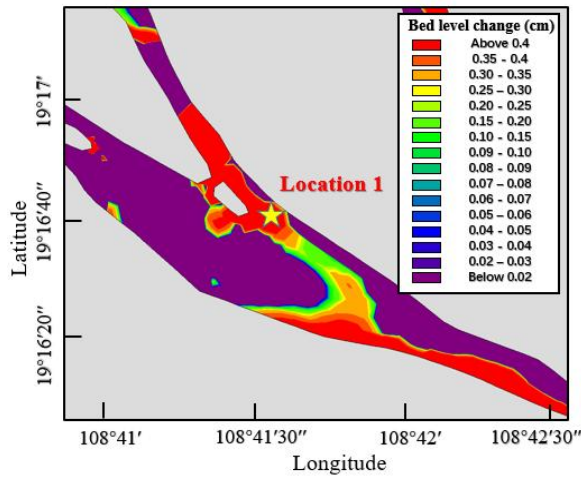
450 In the Danchangcun region, the estuary displays a maximum sediment deposition thickness of 0.59 cm. The presence of a small river island in this area results in shallow deposition near the island, with some areas having thicknesses below 0.3 cm. In contrast, deeper deposition is observed along the riverbanks and particularly near the estuary. The sand mouth at the estuary's entrance is influenced by river erosion and coastal currents, leading to the formation of a new small sand mouth to the southwest. The original sand mouth tends to thicken after fracturing, with scouring at its front end and deposition at the fractured end, reaching a maximum thickness of 0.6 cm. This suggests that the estuary's current is obstructed by multiple depositional strips, resulting in a slower current and increased deposition.

460 In the Xiantiancun region, the estuary is narrower than in Danchangcun, with numerous tributaries dispersing the flow and reducing energy. This leads to varying degrees of deposition at the entrances of the tributaries, although the overall deposition is less than that observed at the Danchangcun mouth. The maximum deposition thickness at the estuary reaches 0.58 cm, with other areas exhibiting thicknesses ranging from 0.3 cm to 0.5 cm. Deposition near the sand mouth contributes to its expansion, and a long silting zone is present at the rear of the river island, characterized by a thin layer over a large area.

5.3 Analysis of deposition in Changhua River channel

Changhua River's channel exhibits two key sediment deposition sites: the Chahe confluence and an area near Jiuxiancun. These areas are prone to significant sedimentation as the river narrows from a wide estuary to a more confined channel, increasing the risk of blockages (Fig. 18a). The primary sedimentation zone is located on the right bank of the distributary, with the maximum thickness measuring 0.47 cm (Fig. 18b). Deposition is most intense around the river island and decreases from the right side towards the rear and the left side of the island. This distribution suggests that sedimentation is more pronounced in the upper, narrower section of the channel.

475 In the main channel, erosion occurs on the ocean-facing right side, while the left side is subject to deposition. The sediments on the left bank are likely sourced from tidal actions or upstream inflows, a process that requires further study. The lateral variation in sedimentation and scouring highlights the intricate sediment dynamics within the river channel.

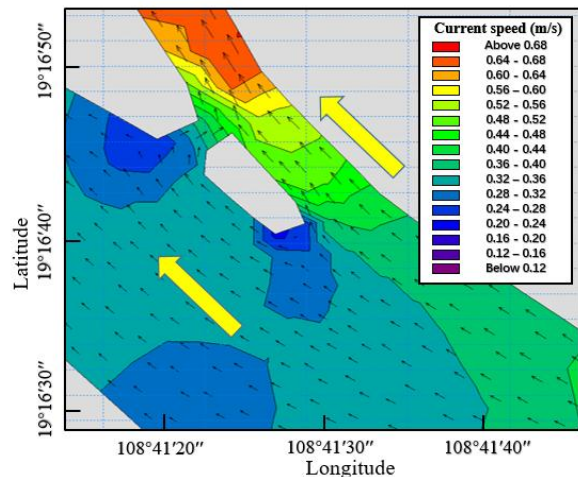
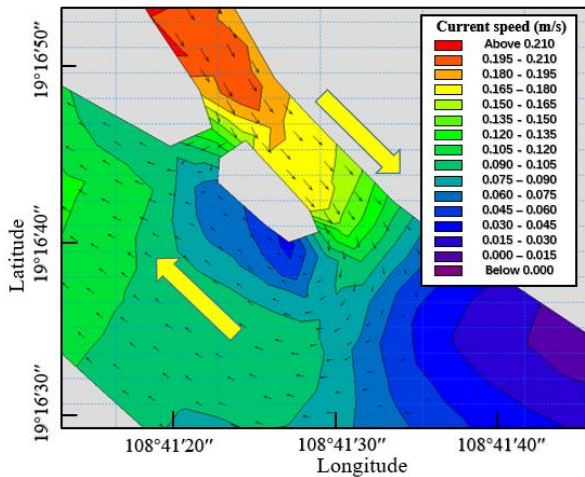


(a)

(b)

Figure 18: Deposition in channel: (a) shows changes of sedimentation thickness of channel with palette; (b) shows changes of sedimentation thickness of channel in detail.

Analysis of topography and flow velocities along the river island banks indicates a pattern of alternating unidirectional and counter-currents (Fig. 19). The current speeds peak at 0.21 m/s during opposing flows and reach approximately 0.68 m/s when currents are in the same direction. The Xiantiancun section, marked by a constricted channel and intensified currents, is prone to sediment accumulation. As tides recede, the river's hydrodynamic energy weakens, facilitating the convergence of the Xiantiancun course with the estuary's incoming flows. This interaction leads to the predominant deposition of sediment on the left bank of the main channel, facing the ocean, which is influenced by high-tide influxes.



(a)

(b)

Figure 19: Flow around the river island: (a) shows the flow around river island in opposite directions; (b) shows the flow around river island in same directions

A secondary sediment deposition site has been identified in proximity to Jiuxiancun, with the maximal sediment thickness measuring 0.81 cm (Fig. 20). This deposition zone is elongated and in close proximity to the coast, while erosion is observed

on the opposing bank. The river's erosive action has led to the removal of the opposite bank, with the displaced sediment accumulating near Jiuxiancun. Over time, this accumulation is expected to enhance the river bend's curvature, potentially
 490 hindering the river's natural evolution.

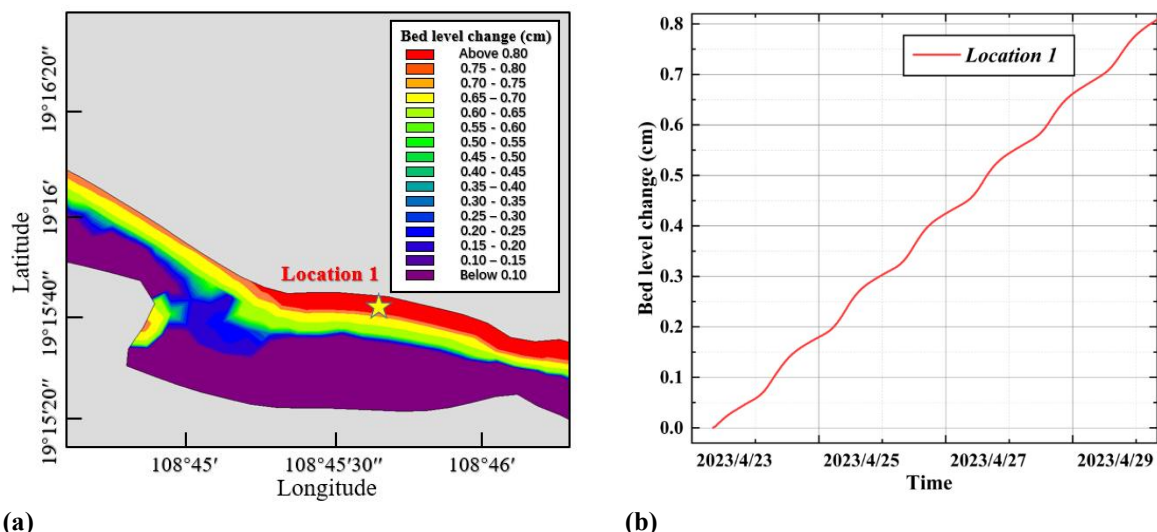


Figure 20: Deposition near the Jiuxiancun: (a) shows changes of sedimentation thickness of Jiuxiancun with palette; (b) shows changes of sedimentation thickness of Jiuxiancun in detail.

To summarise, there are two clear deposits at the channel of the Changhua River. One occurs at the intersection of Xiantiancun and Danchangcun, while the other is near Jiuxiancun. Compared to the fork, sedimentation near the Jiuxiancun
 495 is deeper and thicker. The final deposition thickness of the model is 0.81 cm. The fork was deposited near the river island, and the simulation resulted in a displacement of 0.47 cm. The sediment carried by the high tide may be the source.

6 Discussion

6.1 Residual Current

Residual currents to some extent reflect the transfer and exchange of water bodies, and their direction is usually the direction
 500 of sediment movement and the dispersion and migration of pollutant substances (Robinson, 1983). They are closely related to the long-term transfer and deposition of estuarine materials. Therefore, studying the characteristics of residual currents in this sea area under the combined action of waves and currents can comprehensively understand the evolution characteristics of the sea area's sediment. Tidal residual currents can be studied using the Lagrangian and Eulerian methods. Eulerian
 505 residual current refers to the average transfer caused by the average flow after removing the periodic astronomical tide, and its magnitude and direction mainly depend on the strength and duration of the ebb and flood tidal velocities within the tidal cycle; Stokes' drift characterizes the net drift of the water body, and its numerical size directly reflects the correlation between the tidal range and the change in flow velocity within the tidal cycle, and the sum of the two is the Lagrangian

residual current. The Lagrangian residual current is not the result of the long-term tracking of real particles, but is the result of the superposition of Eulerian residual current and Stokes' drift.

510 Eulerian residual current refers to the average transfer caused by the average flow after removing the periodic astronomical tide, and its magnitude and direction mainly depend on the strength and duration of the ebb and flood tidal velocities within the tidal cycle; Stokes' drift characterizes the net drift of the water body, and its numerical size directly reflects the correlation between the tidal range and the change in flow velocity within the tidal cycle, and the sum of the two is the Lagrangian residual current. The formulas for calculating Eulerian residual current and Stokes' drift refer to previous studies
 515 (Longuet-Higgins, 1969; Uncles and Jordan, 1980; Li and O'Donnell, 1997).

Through the analysis of sediment simulation results from the previous section on the distribution of major sedimentation areas, we have been able to understand the distribution of these areas. However, the causes of sedimentation require further exploration. In this section, based on the tidal current field data from hydrodynamic numerical simulation, we calculate the residual flow according to the entire study area. The flow velocity measured data from two ADCP stations outside the
 520 estuary of the Changhua River was analyzed using the tidal residual current calculation method, thereby enhancing the credibility of the residual flow field.

Table 8 Residual currents in spring neap tide at each station

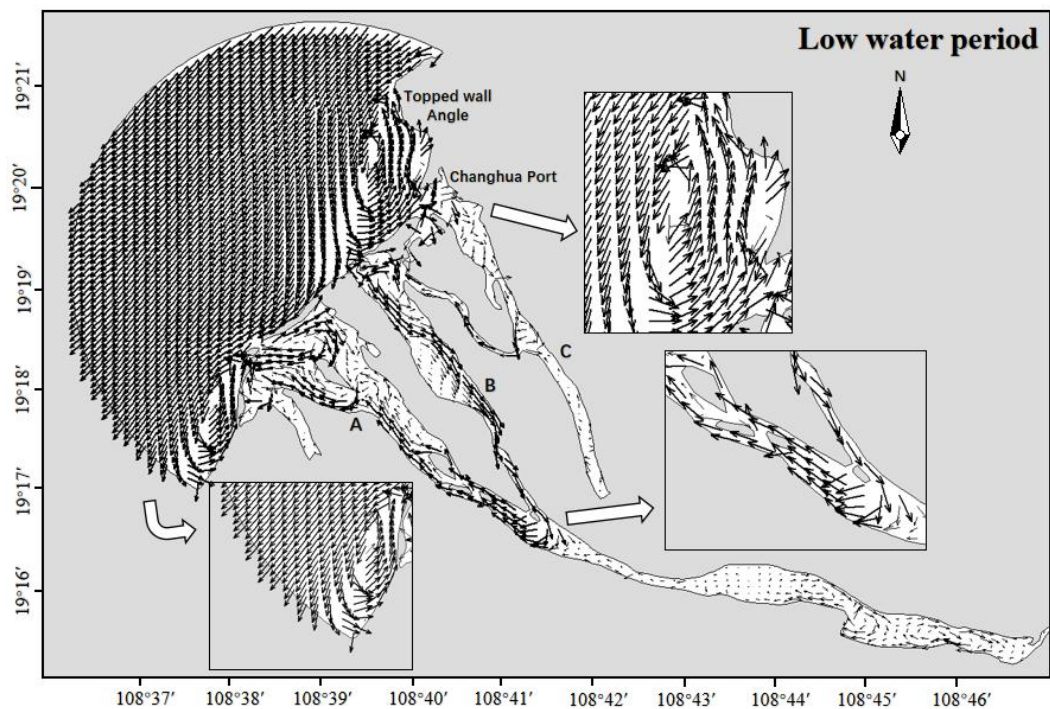
Station	Eulerian residual current		Stokes' drift		Lagrangian residual current	
	Speed (m/s)	Degree (°)	Speed (m/s)	Degree (°)	Speed (m/s)	Degree (°)
ADCP01	0.0913	232	0.0006	172	0.0917	231
ADCP02	0.0331	137	0.0007	194	0.0335	138

The Lagrangian residual current at monitoring station ADCP01 is 0.0913 m/s with a direction of 231° (SW), and at station ADCP02 it is 0.0331 m/s with a direction of 138° (NW) (Table 8). In the area outside the Changhua River estuary, the
 525 Stokes tidal residual current at the monitoring stations is two orders of magnitude smaller than the Eulerian residual current. Therefore, the flow trend of the composite Lagrangian tidal residual current remains essentially consistent with that of the Eulerian residual current.

6.2 Influence of residual current in low water period

The study area has a distinct monsoon climate, with prevailing southerly winds in the summer and alternating southerly and
 530 northeasterly winds in the spring. Figure 21 shows the Eulerian residual current field during the simulation period (low water period). To present the Eulerian residual currents within the study area in a complete and clear manner, a limit on vector length was set when plotting the current field. Consequently, the direction and length of the arrows in the figure represent the direction of the residual currents, but not their intensity. However, the intensity of the Eulerian residual currents can still be discerned through the data at the grid points. The Eulerian residual current outside the Changhua River estuary generally
 535 flows southward. As it flows from north to south, it is obstructed by the sand spit, diverging around it. After the divergence,

the southwestward Eulerian residual current splits, with one part following the sand spit to the river mouth near A, and the other part entering channel B and flowing inward. The northeastward Eulerian residual current, after divergence, encounters the obstruction of the headland (Topped wall Angle) and forms a counterclockwise circulation below Topped wall Angle. Headlands are one of the key topographical features where strong residual current vortices occur (Maddock et al., 1978; 540 Pingree et al., 1977; Smith, 2010). At the headland, the water depth shoals in the onshore direction, and the frictional effect is stronger in shallow water areas than in deep water areas. This results in a frictional force moment on the alongshore tidal current, generating vorticity. The transport of vorticity within the closed circulation lines on either side of the headland is not equal in input and output. After a tidal cycle of time averaging, a net vorticity will be produced on both sides of the headland, forming two counter-rotating residual current vortices, with the tidal residual current at the tip of the headland generally 545 pointing seaward (Zimmerman, 1981). Topped wall Angle, being a headland, can produce similar residual current field results. A clockwise residual current vortex opposite to the one below may exist above Topped wall Angle. The Eulerian residual currents in the three river channels where A, B, and C are located all flow towards the river mouths. The Eulerian residual current in the channel between B and C flows from B to C.



550 **Figure 21: Eulerian residual current field during low water period**

6.3 Influence of residual current in high water period

In order to comprehensively understand the residual current field of the study area, it is essential to analyze the residual current field during the flood season. The figure displays the Eulerian residual current field of the study area for July 2022

(high water period). The Eulerian residual current south of the river mouth in the study area still flows to the south (towards Beili Bay), but the nearshore residual current veers more quickly, resulting in a smaller circulation compared to the dry season. The circulation range in the north has expanded, likely due to the influence of the southerly monsoon during the summer, leading to an increase in the strength and directional deflection of the Eulerian residual current. When it reaches the shore, it is naturally obstructed by the sand spit and disperses to both sides (NE-SW). The upward Eulerian residual current, upon encountering the sea area outside Changhua Port, is deflected by the coastal promontory (Topped wall Angle) and turns westward. The westward Eulerian residual current, continuously affected by the strong southerly winds during its movement, keeps deflecting. Eventually, a circulation is formed, with a circulation range larger than that of the dry season. The situation in channel A is essentially consistent with the dry season, while the Eulerian residual current directions in channel B and C are the same as that in A, all flowing towards the ocean. This is quite different from the dry season, with a flow direction opposite to that of the dry season, which may be related to the increased rainfall and subsequent increase in downstream flow during the summer flood season.

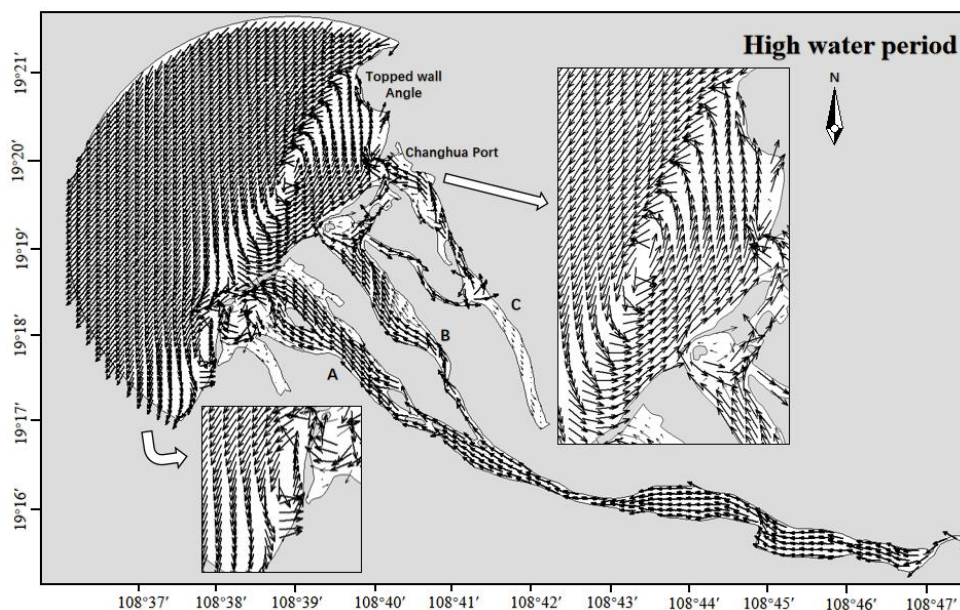


Figure 22: Eulerian residual current field during high water period

7 Conclusions

The study successfully applied a wave-current coupled sediment transport model to the lower reaches of the Changhua River in Hainan Island. By integrating field measurements, remote sensing techniques, and the Van Rijn model, this research has developed a comprehensive model capable of accurately simulating sediment behavior under the combined action of waves and currents. The following conclusions reflect a robust understanding of the study's themes:

The study area's surface sediments consist of ten types, including gravelly sand, sandy gravel, silty gravel, sandy silt, silt, gravelly silt, sand, gravelly sandy silt, gravelly sand, and silty gravelly sand. Among these, gravelly sand and gravelly sand are the predominant types.

575 During the transition from flood to ebb tide, the flow field outside the estuary is driven by the deflection of water currents from Beili Bay and Changhua Port, shifting the flow direction from northeast to southwest. During the transition from ebb to flood tide, the deflection is primarily influenced by the circulation outside Changhua Port, shifting the flow direction from southwest to northeast.

580 The main sedimentation areas within the study area's river channels include Xiantiacun, Danchangcun, and Jiuxiancun. The first two experience sediment deposition near the river mouth's sand spit, while the latter's sediment is primarily deposited near the river bifurcation.

585 Regardless of whether it is the dry season or the flood season, the residual currents in the study area are directed towards Beili Bay (SWS), implying that sediments in the lower reaches of the Changhua River will be influenced by the residual currents and transported towards Beili Bay. The sand spit at the river mouth, affected by the southward residual currents, will cause sediments from the north to be transported towards the northeast and southwest of the sand spit, leading to its elongation. There exists a counterclockwise residual current eddy beneath Topped wall Angle, and it is timed with a clockwise residual current eddy above Topped wall Angle. The river's discharge has little impact on Channel A, but it significantly affects Channels B and C.

590

References

- Adnan, R.M., Liang, Z.M., El-Shafie, A., Zounemat-Kermani, M., Kisi, O.: Prediction of Suspended Sediment Load Using Data-Driven Models, *Water*, 11(10), 2060. doi: 10.3390/w11102060, 2019.
- 595 Addison - Atkinson, W., Chen, A.S., Memon, F.A., Anta, J., Naves, J., Cea, L.: Investigation of uniform and graded sediment wash-off in an urban drainage system: Numerical model validation from a rainfall simulator in an experimental facility, *Journal of Hydrology*, 629, 130561. doi: 10.1016/j.jhydrol.2023.130561, 2024.
- Auguste, C., Nader, J.R., Marsh, P., Cossu, R., Penesis, I.: Variability of sediment processes around a tidal farm in a theoretical channel, *Renewable Energy*, 171, 606-620. doi: 10.1016/j.renene.2021.02.147, 2021.
- 600 Bai, J., Fang, H. W., He, G.J., Xie, C. B., Gao, H.: Numerical simulation of erosion and transport of fine sediments by large eddy simulation. *Chinese Journal of Theoretical and Applied Mechanics*, 49(1), 65-74. doi: 10.6052/0459-1879-16-235, 2017.
- Bakhtyar, R., Barry, D.A., Li, L. Jeng, D. S.: Yeganeh-Bakhtiary, A.: Modeling sediment transport in the swash zone: A review, *Ocean Engineering*, 36, (9-10), 767-783, doi: 10.1016/j.oceaneng.2009.03.003, 2009.

- 605 Blumberg, A. F., Mellor, G. L.: A description of a three-dimensional coastal ocean circulation model. *Coastal and Estuarine Sciences*, 4, 1-16. doi: 10.1029/CO004p0001, 1987.
- Brenna, A., Marchi, L., Borga, M., Zaramella, M., Surian, N.: What drives major channel widening in mountain rivers during floods? The role of debris floods during a high-magnitude event, *Geomorphology*, 430, 108650. doi: 10.1016/j.geomorph.2023.108650, 2023.
- 610 Bui, L. H. N., Bui, L. T.: Modelling bank erosion dependence on natural and anthropogenic factors — case study of Ganh Hao estuary, Bac Lieu - Ca Mau, Vietnam, *Environmental Technology & Innovation*, 19, 100975. doi: 10.1016/j.eti.2020.100975, 2020.
- Bijker, E. W.: Some considerations about scales for coastal models with movable bed, Delft Hydraulics Laboratory publication, 50. doi: <https://repository.tudelft.nl/record/uuid:cdf2f061-3fe6-4361-a0e7-636fc69c9eca>, 1967.
- 615 Chen, W.Q., Werf, J.J., Hulscher, S.J.M.H.: Practical modelling of sand transport and beach profile evolution in the swash zone, *Coastal Engineering*, 191, 104514. doi: 10.1016/j.coastaleng.2024.104514, 2024.
- Chen, C., Liu, H., Beardsley, R. C.: An unstructured grid, finite-volume, three-dimensional, primitive equations ocean model: application to coastal ocean and estuaries. *Journal of atmospheric and oceanic technology*, 20(1): 159-186. doi: 10.1175/1520-0426(2003)020<0159:AUGFVT>2.0.CO;2, 2003.
- 620 Chen, C., Xue, P., Ding, P., Beardsley, R. C., Xu, Q., Mao, X., Gao, G., Qi, J., Li, C., Lin, H., Cowles, G., Shi, M.: Physical mechanisms for the offshore detachment of the Changjiang Diluted Water in the East China Sea. *Journal of Geophysical Research: Oceans*, 113(C2). doi: 10.1029/2006JC003994, 2008.
- Chen, T., Zhang, Q., Wu, Y., Ji, C., Yang, J., Liu, G.: Development of a wave-current model through coupling of FVCOM and SWAN, *Ocean Engineering*, 164, 443-454. doi: 10.1016/j.oceaneng.2018.06.062, 2018.
- 625 Czitrom, V. A.: One-factor-at-a-time versus designed experiments, *American Statistician*, 53 (2), 126-131. doi: 10.1080/00031305.1999.10474445, 1999.
- Claude, N., Rodrigues, S., Bustillo, V., Bréhéret, J.G., Macaire, J.J., Jugé, P.: Estimating bedload transport in a large sand-gravel bed river from direct sampling, dune tracking and empirical formulas, *Geomorphology*, 179, 40-57. doi: 10.1016/j.geomorph.2012.07.030, 2012.
- 630 Clift, P.D., Plumb, R.A.: *The Asian Monsoon: Causes, History and Effects*. Cambridge University Press, 37(3), 92-93. doi: 10.1017/CBO9780511535833, 2008.
- Constant, M., Alary, C., Weiss, L., Constant, A., Billon, G.: Trapped microplastics within vertical redeposited sediment: Experimental study simulating lake and channeled river systems during resuspension events, *Environmental Pollution*, 322, 121212. doi: 10.1016/j.envpol.2023.121212, 2023.
- 635 Doroudi, S., Sharafati, A.: A newly developed multi-objective evolutionary paradigm for predicting suspended sediment load, *Journal of Hydrology*, 634, 131090. doi: 10.1016/j.jhydrol.2024.131090, 2024.
- Ding, Q.L.: Wave characteristics and calculation of Beibu Gulf. *Marine Forecasts*, 7 (2): 46-52. doi: 10.11737/j.issn.1003-0239.1990.02.007, 1990.

- Fang, X., Zou, J., Wu, Y., Zhang, Y., Zhao, Y., Zhang, H.: Evaluation of the sustainable development of an island “Blue Economy”: a case study of Hainan, China. *Sustainable Cities and Society*, 66, 102662. doi: 10.1016/j.scs.2020.102662, 2021.
- 640 Feng, H.L., Liu, M., Xu, M.Y., Zhang, M.X., Mo, L., Chen, T., Tan, X.Y., Liu, Z.Y.: Study on the integrated protection strategy of water environment protection: The case of Hainan Province of China. *Environmental Technology & Innovation*, 24, 101990. doi: 10.1016/j.eti.2021.101990, 2021.
- Gao, J.: Study on sediment transport model in Changhua River Estuary of Hainan Province based on remote sensing analysis. China University of Geosciences (Beijing). doi: CNKI: CDMD: 2.1014.101980080086, 2014.
- 645 Gessler, D., Hall, B., Spasojevic, M., Holly, F. M., Pourtaheri, H., Rappelt, N. X.: Application of 3D mobile bed, hydrodynamics model. *Journal of Hydraulic Engineering*, 125(7), 737-749. doi: 10.1061/(ASCE)0733-9429(1999)125:7(737), 1999.
- Han, X.J., Kuang, C.P., Gong, L.X., Li, W.B.: Sediment transport and seabed evolution under artificial headland and beach nourishment engineering. *Oceanologia et Limnologia Sinica*, 53(4), 917-932. doi: 10.11693/hyhz20211200345, 2022.
- 650 Holly, F. M., Rahuel, J. L.: New numerical/physical framework for mobile-bed modeling. Part 1: Numerical and physical principles. *Journal of Hydraulic Research*, 28(4), 401-416. doi: 10.1080/00221689009499057, 1990.
- Hu, X.Z.: Mathematical Simulation Study of Sediment in Intake and Outfall of Dongfang (East) Power Plant in Hainan at North Bay. *Pearl River*, 030 (006): 18-23. doi: 10.3969/j.ISSN.1001-9235.2009.06.006, 2009.
- 655 Huang, H., Chen, C., Blanton, J. O., Andrade, F. A.: A numerical study of tidal asymmetry in Okatee Creek, South Carolina. *Estuarine, Coastal and Shelf Science*, 78(1): 190-202. doi: 10.1016/j.ecss.2007.11.027, 2008.
- Jia, Y., Wang, S. S.: Numerical model for channel flow and morphological change studies. *Journal of Hydraulic Engineering*, 125(9), 924-933. doi: 10.1061/(ASCE)0733-9429(1999)125:9(924), 1999.
- Jin, J., Ou-Yang, Z.Y., Lin, S.K., Wang, X.K.: A study on ecosystem deterioration and protection counter-measure of Hainan Island coast. *Ocean Development and Management*, 2008(1), 103-108. doi: 10.20016/j.cnki.hykyfjgl.2008.01.022, 2008.
- 660 Jiang, L., Xia, M.: Dynamics of the Chesapeake Bay outflow plume: Realistic plume simulation and its seasonal and interannual variability. *Journal of Geophysical Research: Oceans*, 121(2): 1424-1445. doi: 10.1002/2015JC011191, 2016.
- Ji, C., Zhang, Q., Ma, D., Wu, Y., Jiang, Q.: Nearshore coupled wave-current model based on new three-dimensional radiation stress formulation. *Journal of Zhejiang University (Engineering Science)*, 56(1), 128-136. doi: 10.3785/j.issn.1008-973X.2022.01.014.
- 665 Leary, K.C.P., Buscombe, D.: Estimating sand bed load in rivers by tracking dunes: a comparison of methods based on bed elevation time series, *Earth Surface Dynamics*, 8, 161-172. doi: 10.5194/ESURF-8-161-2020, 2020.
- Lee, H. Y., Hsieh, H. M., Yang, J. C., Yang, C. T.: Quasi-two-dimensional simulation of scour and deposition in alluvial channels. *Journal of Hydraulic Engineering*, 123(7), 600-609. doi: 10.1061/(ASCE)0733-9429(1997)123:7(600), 1997.
- 670 Liu, J., Bai, Y.C.: The interactions between wave and cohesive sediment. *Mechanics in Engineering*, 36(3), 253-260. doi: 10.6052/1000-0879-13-204, 2014.

- Lai, W., Pan, J., Devlin, A. T.: Impact of tides and winds on estuarine circulation in the Pearl River Estuary. *Continental Shelf Research*, 168, 68-82. doi: 10.1016/j.csr.2018.09.004, 2018.
- 675 Longuet-Higgins, M.S.: On the transport of mass by time-varying ocean currents. *Deep Sea Research and Oceanographic Abstracts*, 16(5), 431-447. doi: 10.1016/0011-7471(69)90031-X, 1969.
- Li, C., O'Donnell, J.: Tidally driven residual circulation in shallow estuaries with lateral depth variation. *Journal of Geophysical Research*, 102(C13), 27915–27929, doi: 10.1029/97JC02330. 1997.
- Mao, L.M., Zhang, Y.L., Bi, H.: Modern pollen deposits in coastal mangrove swamps from northern Hainan Island, China. *Journal of Coastal Research*, 22 (6), 1423-1436. doi: 10.2112/05-0516.1, 2006.
- 680 Michel, G., Le Bot, S., Deloffre, J., Legrain, M., Levallant, R., Simon, M., Tessier, B., Lesourd, S.: In-situ characterisation of fluvial dune morphology and dynamics under limited sediment supply conditions, Seine River, France, *Geomorphology*, 439, 108855. doi: 10.1016/j.geomorph.2023.108855, 2023.
- Miluch, J., Maciąg, L., Osadczyk, A., Harff, J., Jiang, T., Chen, H.J., Krzysztof Borówka, R., Kevin-McCartney.: *Multivariate geostatistical modeling of seismic data: Case study of the Late Pleistocene paleodelta architecture (SW off-shore Hainan Island, south China sea)*, *Marine and Petroleum Geology*, 136, 105467. doi: 10.1016/j.marpetgeo.2021.105467, 2022.
- 685 Ministry of Water Resources of the People's Republic of China: Code for design of river regulation. Ministry of Housing and Urban-Rural Development of the People's Republic of China State Administration of Quality Supervision, GB 50707-2011, 2011.
- 690 Mohd-Salleh, S.H., Ahmad, A., Wan-Mohtar, W.H.M., Lim, C.H., Abdul-Maulud, K.N.: Effect of projected sea level rise on the hydrodynamic and suspended sediment concentration profile of tropical estuary, *Regional Studies in Marine Science*, 24, 225-236. doi:10.1016/j.rsma.2018.08.004, 2018.
- Maddock, L., Pingree, R.D.: Numerical simulation of the Portland tidal eddies. *Estuarine and Coastal Marine Science*, 6(4), 353-363. doi: 10.1016/0302-3524(78)90127-5, 1978.
- 695 Nash, J.E., Sutcliffe, J.V.: River flow forecasting through conceptual models part I — A discussion of principles, *Journal of Hydrology*, 10 (3), 282-290. doi: 10.1016/0022-1694(70)90255-6, 1970.
- Niu, J., Xie, J., Lin, S., Lin, P., Gao, F., Zhang, J., Cai, S.: Importance of bed liquefaction-induced erosion during the winter wind storm in the Yellow River Delta, China, *Journal of Geophysical Research: Oceans*, 128(10), e2022JC019256. doi: 10.1029/2022JC019256, 2023.
- 700 Nowacki, D.J., Grossman, E.E.: Sediment transport in a restored, river-influenced Pacific Northwest estuary. *Estuarine, Coastal and Shelf Science*, 242, 106869. doi: 10.1016/j.ecss.2020.106869, 2020.
- Orseau, S., Huybrechts, N., Tassi, P., Pham Van Bang, D., Klein, F.: Two-dimensional modeling of fine sediment transport with mixed sediment and consolidation: Application to the Gironde Estuary. *International Journal of Sediment Research*, 36(6), 736-746. doi: 10.1016/j.ijsrc.2019.12.005, 2021.
- 705

- Papanicolaou, A., Bdour, A., Wicklein, E.: One-dimensional hydrodynamic/sediment transport model applicable to steep mountain streams. *Journal of Hydraulic Research*, 42(4), 357-375. doi: 10.1080/00221686.2004.9728402, 2004.
- Pingree, R.D., Maddock, L.: Tidal residuals in the English Channel. *Journal of the Marine Biological Association of the United Kingdom*, 57, 339-354. doi: 10.1017/S0025315400021792, 1977.
- 710 Pradhan, U.K., Mishra, P., Mohanty, P.K., Panda, U.S., Ramanamurthy, M.V.: Modeling of tidal circulation and sediment transport near tropical estuary, east coast of India. *Regional Studies in Marine Science*, 37, 101351. doi: 10.1016/j.rsma.2020.101351, 2020.
- Qi, Y.L., Yu, Q., Gao, S., Li, Z.Q., Fang, X., Guo, Y.H.: Morphological evolution of river mouth spits: Wave effects and self-organization patterns. *Estuarine, Coastal and Shelf Science*, 262, 107567. doi: 10.1016/j.ecss.2021.107567, 2021.
- 715 Robinson, I. S.: Chapter 7 Tidally Induced Residual Flows. *Elsevier Oceanography*, 35: 321-356. doi: 10.1016/S0422-9894(08)70505-1, 1983.
- Sarwar, S., Borthwick, A.G.L.: Estimate of uncertain cohesive suspended sediment deposition rate from uncertain floc size in Meghna estuary, Bangladesh. *Estuarine, Coastal and Shelf Science*, 281, 108183. doi: 10.1016/j.ecss.2022.108183, 2023.
- Spasojevic, M., Holly, F.M.: 2-D bed evolution in natural watercourses—new simulation approach. *Journal of Waterway, 720 Port, Coastal, and Ocean Engineering*, 116(4), 425-443. doi: 10.1061/(ASCE)0733-950X(1990)116:4(425), 1990.
- Team S.: SWAN Cycle III Version 40.51 User Manual. Delft University of Technology, Faculty of Civil Engineering and Geosciences, Environmental Fluid Mechanics Section, Delft, Netherlands, doi: 5944650/user-manual-swan-cycle-iii-version-40.51, 2006.
- Smith, P.C.: The Mean and Seasonal Circulation off Southwest Nova Scotia. *Journal of Physical Oceanography*, 13, 1034-725 1054. doi: 10.1175/1520-0485(1983)013<1034:TMASCO>2.0.CO;2, 1983.
- Terêncio, D.P.S., Pacheco, F.A.L., Valle-Junior, R.F., Melo-Silva, M.M.A.P., Pissarra, T.C.T., Melo, M.C., Valera, C.A., Fernandes, L.F.S.: The Igarapé Weir decelerated transport of contaminated sediment in the Paraopeba River after the failure of the B1 tailings dam (Brumadinho). *International Journal of Sediment Research*, 38(5), 673-697. doi: 10.1016/j.ijsrc.2023.06.004, 2023.
- 730 Thomas, W.A., Prashum, A.I.: Mathematical model of scour and deposition. *Journal of the Hydraulics Division*, 103(8), 851-863. doi: 10.1061/JYCEAJ.0004805, 1977.
- Uncles, R.J., Jordan, M.B.: A one-dimensional representation of residual currents in the Severn Estuary and associated observations. *Estuarine and Coastal Marine Science*, 10(1), 39-60. doi: 10.1016/S0302-3524(80)80048-X, 1980.
- Van-Rijn, L.C.: Sediment Transport, Part I : Bed load transport. *Journal of Hydraulic Engineering*, 110(10), 1431-1455. doi: 735 10.1061/(ASCE)0733-9429(1984)110:10(1431), 1984.
- Vázquez-Tarrió, D., Ruiz-Villanueva, V., Garrote, J., Benito, G., Calle, M., Lucía, A., Díez-Herrero, A.: Effects of sediment transport on flood hazards: Lessons learned and remaining challenges, *Geomorphology*, 446, 108976. doi: 10.1016/j.geomorph.2023.108976, 2024.

- Vinzon, S.B., Gallo, M.N., Gabioux, M., Fonseca, D.L., Achete, F.M., Ghisolfi, R.D., Mill, G.N., Fonseca, S.A.R., Silva-Quaresma, V., Oliveira, K.S.S., Brigagão, G., Machado, L.G.: The role of waves in the resuspension and transport of fine sediment and mine tailings from the Fundão Dam failure, Doce River, Brazil, *International Journal of Sediment Research*, 39(1), 44-60. doi: 10.1016/j.ijsrc.2023.09.004, 2023.
- 740 Wang, D., Pei, L., Zhang, L., Li, X., Chen, Z., Zhou, Y.: Water resource utilization characteristics and driving factors in the Hainan Island. *Journal of Groundwater Science and Engineering*, 11(2), 191-206. doi: 10.26599/JGSE.2023.9280017, 2023.
- 745 Wang, X.M., Qu, H.B., Xiong, Y.K., Lu, L., Hu, K.: Grain-size characteristics and transport trend of bottom sediments at the estuary of Changhua River in Hainan. *Geoscience*, 36 (1), 88-95. doi: 10.19657/j.geoscience.1000-8527.2021.1720001106, 2022.
- Wang, Y.: Environmental characteristics of Hainan Island coast. *Marine Geology letters*, 18(3), 1-9. doi: CNKI:SUN:HYDT.0.2002-03-000, 2002.
- 750 Wang, X.H.: Analysis of wave characteristics in the offshore area of Dongfang City. *Marine Sciences*, 47(2), 31-46. doi:10.11759/hyxx20220919001, 2023.
- Wu, J.Q., Xiao, M., Yang, J.T., Xiao, X.B., Tang, W.H.: Study on distribution characteristics of soil erosion in the lower reaches of Changhua River in Hainan. *Technology of Soil and Water Conservation*, 2012(3), 12-15. doi: 10.3969/j.issn.1673-5366.2012.03.04, 2012.
- 755 Wu, W., Rodi, W., Wenka, T.: 3D numerical modeling of flow and sediment transport in open channels. *Journal of Hydraulic Engineering*, 126(1), 4-15. doi: 10.1061/(ASCE)0733-9429(2000)126:1(4), 2000.
- Yang, Z.H., Jia, J.J., Wang, X.K., Gao, J.H.: Characteristics and variations of water and sediment fluxes into the sea of the top three rivers of Hainan in recent 50 years. *Marine Science Bulletin*, 32 (1), 92-99. doi: 10.11840/j.issn.1001-6392.2013.01.014, 2013.
- 760 Zeng, Z.X., Zeng, X.Z.: *Physicogeography of Hainan Island*. Science Press, Beijing, 1989.
- Zhang, L.M., Wei, Z.Y., Cao, Q.M., Sang, A.Y., Wang, H., Qi, Z.P.: Characteristics and influencing factors of sediment concentration in the lower reaches of three major rivers in Hainan Province in recent 40 years. *Ecology and Environmental Sciences*, 15(4), 765–769. doi: 10.3969/j.issn.1674-5906.2006.04.022, 2006.
- Zhang, P., Ruan, H.M., Dai, P.D., Zhao, L.R., Zhang, J.B.: Spatiotemporal river flux and composition of nutrients affecting adjacent coastal water quality in Hainan Island. *Journal of Hydrology*, 591, 125293. doi: 10.1016/j.jhydrol.2020.125293, 2020.
- 765 Zhang, W.Y., Xiong, P., Meng, Q.C., Dudzinska-Nowak, J., Chen, H., Zhang, H., Zhou, F., Miluch, J., Harff, J.: Morphogenesis of a late Pleistocene delta off the south-western Hainan Island unraveled by numerical modeling, *Journal of Asian Earth Sciences*. 195, 104351. doi: 10.1016/j.jseaes.2020.104351, 2020.
- 770 Zhao, L., Cai, G.Q., Zhong, H.X., Li, B., Zou, L.Q., Li, S., Han, Y.F.: Grain-size characteristics and sedimentary environment of surface sediments in the shallow sea in the southeast of Hainan Island. *Marine Geology & Quaternary Geology*, 41(2), 64-74. doi: 10.6562/j.cnki.5566-1992585866, 2021.

Zhu, L.R., Liu Y.H., Ye, C.Q.: Runoff change and influencing factors of Changhua River in arid area of Hainan Island. *Ecological Science*, 39 (1), 183-189. doi: CNKI: Sun: STKX.0.2020-01-023, 2020.

775 Zimmerman, J.: Dynamics, diffusion and geomorphological significance of tidal residual eddies. *Nature*, 290, 549–555. doi: 10.1038/290549a0, 1981.